Petrogenesis and tectonic setting of mid-Neoproterozoic low-$\delta^{18}O$ metamafic rocks from the Leeuwin Complex, southwestern Australia

Shihang Yu[a,b,c], Xiaochun Liu[a,c]*, Bin Fu[d], Ian C.W. Fitzsimons[e], Longyao Chen[a,c], Wei-(RZ) Wang[a,c], Yuxing Lou[a,c], Biao Song[f]

[a] *Institute of Geomechanics, Chinese Academy of Geological Sciences, Beijing 100081, China*
[b] *School of Earth and Space Sciences, Peking University, Beijing 100871, China*
[c] *Laboratory of Paleomagnetism and Tectonic Reconstruction, Ministry of Natural Resources, Beijing 100081, China*
[d] *Research School of Earth Sciences, The Australian National University, Canbarra, ACT 2601, Australia*
[e] *School of Earth and Planetary Sciences, Curtin University, Perth, WA 6845, Australia*
[f] *Beijing SHRIMP Centre, Institute of Geology, Chinese Academy of Geological Sciences, Beijing 100037, China*

Revised manuscript submitted to **Precambrian Research**

(October 28, 2021)

*Corresponding author: Xiaochun Liu
Address: Institute of Geomechanics
Chinese Academy of Geological Sciences
11 Minzudaxue Nanlu
Beijing 100081
P. R. China
Tel: +86-10-88815038
Fax: +86-10-68422326
E-mail: liuxchqw@cags.ac.cn; liuxchqw@sina.com

Abstract

Mid-Neoproterozoic low-$\delta^{18}O$ metamafic rocks from the Leeuwin Complex, southwestern Australia, are reported for the first time. Sensitive high-resolution ion microprobe (SHRIMP) zircon U–Pb dating of these upper amphibolite- to granulite-facies mafic rocks yields igneous protolith ages of 674–660 Ma. The metamafic rocks are generally classified as subalkaline tholeiitic rocks with an ocean island basalt (OIB) affinity. They have low Mg# values (22–50) and Cr (0.19–105 ppm) and Ni (0.62–115 ppm) contents, with whole-rock $\varepsilon_{Nd}(t)$ values of −1.4 to +1.5 and zircon $\varepsilon_{Hf}(t)$ values of −0.3 to +3.5. Using these data in combination with the incompatible trace element characteristics, it is inferred that the protoliths of the rocks were derived from low-degree partial melting of relatively depleted asthenospheric mantle in a continental rift environment, and the magmas underwent some crustal contamination and fractional crystallization of mafic minerals. Zircon cores from the metamafic rocks yield $\delta^{18}O$ values of 0.89 to 4.10‰, which are lower than normal mantle values (5.3 ± 0.3‰). These cores preserve oscillatory zoning or banding in cathodoluminescence images, and individual samples have concordant ages and preserve a narrow range of $\delta^{18}O$ values, suggesting that the low-$\delta^{18}O$ signatures are of primary magmatic origin. It is inferred that these low-$\delta^{18}O$ metamafic rocks were generated by contamination by low-$\delta^{18}O$ felsic crustal wall rocks and interaction of the magma with surface water at shallow depths in an extensional regime during the mid-Neoproterozoic.

Keywords: Neoproterozoic; Low-δ^{18}O rocks; Continental rift; Leeuwin Complex; Crustal contamination

1. Introduction

Low-δ^{18}O rocks, those with δ^{18}O values lower than the normal mantle values of 5.3 ± 0.3‰ (Valley et al., 1998), are volumetrically rare on Earth (Balsley and Gregory, 1998; Valley et al., 2005; Zheng et al., 2008; Zhang and Zheng, 2011; Troch et al., 2020). In general, oxygen isotope fractionation is negligible (<0.3‰) during magmatic processes such as fractional crystallization and partial melting (Zhao and Zheng, 2003; Bindeman et al., 2004; Bindeman, 2008). The generation of low-δ^{18}O rocks requires interaction with one of two low-δ^{18}O natural reservoirs, namely seawater (~0‰) or meteoric water (typically negative), at relatively high temperatures (Bindeman and Valley, 2001; Hoefs, 2009; Bindeman and Serebryakov, 2011). Therefore, low-δ^{18}O rocks can provide important information regarding the exchange of material and energy between the interior and exterior of the Earth, and are thus useful paleoclimate indicators (Bindeman and Valley, 2001; Zheng et al., 2004, 2007a, 2008; Fu et al., 2013; He et al., 2016).

A growing number of localities containing low-δ^{18}O rocks have been identified worldwide, and most are Neoproterozoic igneous rocks, including numerous igneous and metaigneous rocks along the northern margin of the South China Block (Zheng et al., 2004, 2006, 2007a, 2007b, 2008; Chen et al., 2011; Fu et al., 2013; Liu et al., 2013; Liu and Zhang, 2013; He et al., 2016; Wu et al., 2020), the Malani igneous suite in northwestern India (Wang et al., 2017), the Seychelles granites (Tucker et al., 2001; Harris and Ashwal, 2002; Zhou et al., 2020), and the Imorona–Itsindro Suite in central Madagascar (Archibald et al., 2016; Zhou et al., 2018). It has been demonstrated that extensional settings, such as continental rifts or calderas, are the ideal tectonic environment to produce low-$\delta^{18}O$ magmas due to well-developed fault systems and extremely high thermal gradients, which facilitate continuous high-temperature reactions between magmas and low-$\delta^{18}O$ fluids (Zheng et al., 2004, 2007a; Zhang and Zheng, 2011; Troch et al., 2020).

In this contribution, we report for the first time low-$\delta^{18}O$ zircons in Neoproterozoic upper amphibolite- to granulite-facies mafic rocks from the Leeuwin Complex, southwestern Australia. Using an integrated study combining zircon U–Pb ages, zircon Hf–O isotopic compositions, whole-rock geochemistry and Nd isotopic data for these rocks, we investigate: (1) the emplacement ages of the protoliths; (2) the petrogenesis and tectonic setting of the metamafic rocks and the nature of their magma source; and (3) the low-$\delta^{18}O$ signatures of these rocks and their petrogenesis. The low-$\delta^{18}O$ mafic magmatic event is coeval with the global extensive rift-related magmatism during the mid-Neoproterozoic (820–620 Ma). Thus, the origin of low-$\delta^{18}O$ mafic magmatism in the Leeuwin Complex might be related to the breakup of the Rodinia supercontinent.

2. Geological background and sample descriptions

2.1. Geological background

The Pinjarra Orogen, located along the western coast of Western Australia, trends N–S and stretches for over 1000 km along the western margin of the Archean Yilgarn Craton to the Proterozoic Albany–Fraser Orogen in the south (Fig. 1a). The Precambrian crystalline basement rocks of the Pinjarra Orogen are poorly exposed, and most are buried beneath the Southern Carnarvon and Perth Basins. Three Precambrian inliers of the Pinjarra Orogen are exposed as, from north to south, the Northampton, Mullingarra and Leeuwin complexes, which include some mafic rocks (Myers, 1990, Wilde and Murphy, 1990; Wingate and Giddings, 2000; Janssen et al., 2003).

The Leeuwin Complex, which is located ~200 km south of Perth, is the southernmost exposed Precambrian basement of the Pinjarra Orogen (Fig. 1b), and is separated from the Phanerozoic Perth Basin by the Dunsborough fault in the west. The basement rocks occur mainly along a narrow coastal strip between Cape Naturaliste in the north and Cape Leeuwin in the south (Fig. 2). Unlike the Northampton and Mullingarra complexes in the northern Pinjarra Orogen, which are composed mainly of paragneisses, the Leeuwin Complex is predominantly made up of upper amphibolite- to granulite-facies felsic orthogneisses with minor meta-anorthosites and layered metamafic rocks (Wilde and Murphy, 1990).

The Leeuwin Complex can be subdivided into northern, central and southern domains on the basis of petrographic and geochronological data (Janssen et al., 2004; Janssen and Fitzsimons, 2005; Fig 2). The northern domain, from Dunsborough to Cape Mentelle, is composed mainly of syenogranitic gneiss and hornblende–biotite granitic gneiss. The southern domain extends from Cosy Corner southwards to Cape Leeuwin, and consists mainly of syenogranitic gneiss and hornblende–biotite granitic gneiss with minor meta-anorthosite cropping out near Augusta. These two domains preserve similar structural styles that are characterized by N–S–trending folds with gently plunging hinges (Collins, 2003; Janssen et al., 2004). Sensitive high–resolution ion microprobe (SHRIMP) U–Pb zircon data from felsic orthogneisses within these two domains yielded protolith ages of 800–650 Ma and metamorphic ages of 530–520 Ma (Nelson, 1996, 1999, 2002; Collins, 2003; Arnoldi, 2017). In contrast, the central domain, located near Redgate Beach, is dominated by migmatized garnet-bearing felsic orthogneiss with relatively flat–lying high-strain foliations (Janssen et al., 2003, 2004; Janssen and Fitzsimons, 2005). These orthogneisses have magmatic crystallization ages of ca. 1090 Ma and metamorphic ages of ca. 1080 and 550–530 Ma (Nelson, 1999; Bodorkos et al., 2016; Arnoldi, 2017).

Metamafic rocks are sparsely distributed throughout the Leeuwin Complex (Fig. 2). These rocks commonly occur as layers, boudins, lenses, or small pods within the felsic orthogneisses, and range from 2 cm to 50 m in width. Their orientations are roughly parallel to the foliation in the host country rocks (Fig. 3a–c). Wilde and Murphy (1990) reported that the metamafic rocks show a general northward increase in metamorphic grade, from upper amphibolite-facies to granulite-facies, and peak metamorphic conditions reached 690 °C and 0.5 GPa. However, the emplacement age, petrogenesis, and geodynamic significance of the rocks are still poorly constrained. Simons (2001) obtained a SHRIMP zircon U–Pb age of 536 ± 21 Ma for a mafic granulite at Shelley Beach, interpreted as the crystallization age of the protolith. However, this age was argued to represent a maximum age for granulite facies metamorphism in the northern Leeuwin Complex (Janssen et al., 2003). Limited geochemical data suggest that the protoliths of the metamafic rocks might have formed in a within-plate setting (Wilde and Murphy, 1990). This is in contrast to modern plate-tectonic reconstructions that have the region in a continental margin setting throughout the Neoproterozoic (Powell and Pisarevsky, 2002; Collins and Pisarevsky, 2005; Merdith et al., 2017, 2021).

2.2. Sample descriptions

To determine the protolith ages and petrogenesis of the metamafic rocks, twelve representative samples of mafic granulites and amphibolites from the Leeuwin Complex were chosen for SHRIMP U–Pb zircon dating and elemental and isotopic analyses. The sample localities are shown in Fig. 2, and lithological, mineral assemblage, and geochronological data are summarized in Table 1.

Six mafic granulite samples collected from the northern Leeuwin Complex are greyish-green to black in colour and fine- to coarse-grained with gneissic structures. They consist predominantly of clinopyroxene, brown hornblende, plagioclase, and opaque minerals, with or without garnet, orthopyroxene, biotite, K-feldspar, and quartz (Table1; Fig. 3d). Garnet from sample D26-2 occurs as relict grains surrounded by plagioclase, which is suggestive of decompression.

Six amphibolite samples collected from the southern Leeuwin Complex are dark-grey in colour and medium-grained with a gneissic structure defined by a preferred orientation of amphibole and plagioclase (Fig. 3e, f). They are composed chiefly of brown to green hornblende, biotite, plagioclase, and opaque minerals, with or without garnet, clinopyroxene, quartz, and titanite (Table 1; Fig. 3e, f). Minor orthopyroxene surrounds opaque minerals in sample D34-5. Garnet from samples D34-5, D34-11, and D34-12 occurs as relict grain surrounded by plagioclase.

3. Analytical methods

3.1. Zircon U–Pb dating and O isotope analyses

Zircon U–Th–Pb isotope analyses were carried out on the SHRIMP II at the Beijing SHRIMP Centre, Chinese Academy of Geological Sciences, Beijing, China. Prior to analysis, zircons were separated from samples using conventional techniques, including crushing, sieving, heavy liquid and hand picking, and then mounted in an epoxy disc along with the TEMORA zircon standard and polished to expose grain centres. High-resolution cathodoluminescence (CL) images were taken to reveal internal structures. For the SHRIMP analyses, the instrumental conditions and data acquisition procedures are similar to those described by Williams (1998). A primary O_2^- ion beam of 4.5 nA, 10 Kv and ~25 μm spot was used. Five scans through the mass stations were made for each age determination. The measured $^{206}Pb/^{238}U$ ratios were calibrated against reference zircon TEMORA (416.75 ± 0.24 Ma; Black et al., 2003). Correction for common Pb was made using the measured ^{204}Pb concentration. Age calculations and concordia diagrams were produced using the SQUID 1.03 (Ludwig, 2001) and ISOPLOT 3.23 (Ludwig, 2003) programs. The age uncertainties for individual analyses are given at one standard deviation (1σ), and the calculated weighted mean $^{206}Pb/^{238}U$ ages are quoted at a 95% confidence level. The analytical data are listed in Table 2.

Following U–Pb analysis, zircon O isotope measurements were performed using the SHRIMP SI (stable isotope) at the Research School of Earth Sciences (RSES), The Australian National University (ANU), Canberra, Australia. Details of the analytical procedures and conditions are similar to those of Ickert et al. (2008) and Fu et al. (2015). The locations of ion microprobe pits for O isotopes were the same as for SHRIMP U–Pb analyses after gentle repolishing. Calibrated $^{18}O/^{16}O$ ratios are reported in $\delta^{18}O$ notation as per-mil variations relative to Vienna standard mean ocean water (VSMOW). The values of $\delta^{18}O$ were calibrated against standard zircon FC-1 ($\delta^{18}O_{VSMOW}$ = 5.61 ± 0.14‰, 2σ, n = 6; Fu et al., 2015). The external spot-to-spot precision was better than ±0.78‰ (n = 103, 2σ).

3.2. Zircon Lu–Hf isotope analyses

Zircon Lu–Hf isotope analyses were conducted using a 193 nm excimer laser-based HELEX ablation system equipped with a Neptune multiple collector inductively coupled plasma mass spectrometer (LA–MC–ICP–MS) at the RSES, ANU. Zircon Hf isotopes were analyzed after ion microprobe O isotope and U–Pb analyses, and on the same analysis domains. Detailed analytical methods are similar to those described by Hiess et al. (2009) using a laser spot size of ~40 μm, and an ablation time of up to 60 s. The isobaric interference correction protocols of ^{176}Lu and ^{178}Yb on ^{176}Hf are described in Woodhead et al. (2004). The ^{176}Yb/^{177}Hf ratio was calculated using the natural ^{176}Yb/^{173}Yb ratio of 0.79502. All results were calibrated against standard zircons 91500, FC-1, Mud Tank, QGNG, Plešovice (Woodhead et al., 2004; Woodhead and Hergt, 2005; Sláma et al., 2008) and synthetic grains (Fisher et al., 2011). Average (± 2σ) measurements on the zircon standards during one of the analytical sessions were: 0.282284 ± 0.000052 (n = 25) for 91500; 0.282163 ± 0.000042 (n = 21) for FC-1; 0.282502 ± 0.000027 (n = 8) for Mud Tank; 0.282459 ± 0.000028 (n = 23) for Plešovice; 0.281603 ± 0.000015 (n = 6) for QGNG.

3.3. Whole-rock geochemical analyses

Whole-rock geochemical analyses were carried out at the National Research Center for Geoanalysis, Chinese Academy of Geological Sciences, Beijing, China. Prior to analysis, all samples were washed and trimmed to remove weathered surfaces. Fresh portions were then pulverized to ~200 mesh in an agate mill. Major element abundances were determined by X-ray fluorescence (XRF, PANalyical Axios PW4400) using fusion beads formed by melting sample powders with a lithium tetraborate flux, except for FeO, H_2O^+, and CO_2 that were measured by wet chemical, combustion, and gas volume methods, respectively. Relative standard deviations of these analyses are within 5%. The trace elements, including rare earth elements (REEs), were conducted by inductively coupled plasma–mass spectrometry (ICP–MS, PE300Q); detailed sample preparation and analytical procedures followed Wang et al. (2003). The detection limit for trace element analysis is ~0.05 ppm. Analytical uncertainties are <5% for trace elements with concentrations of ≥20 ppm, and 5%–10% for elements with concentrations of ≤20 ppm.

3.4. Whole-rock Sm–Nd isotope analyses

Whole-rock Sm–Nd isotope analyses were conducted using a Neptune Plus MC–ICP–MS (Thermo Fisher Scientific, Dreieich, Germany) at Wuhan Sample Solution Analytical Technology Co., Ltd., Hubei, China. Prior to analysis, ~100 mg powders (200 mesh) of each sample were dissolved using HF + HNO_3 acid in Teflon bombs at ~190 °C for >24 hours. Detailed analytical procedures are described by Lin et al. (2016). The Nd measurements were corrected for mass fraction by normalization to $^{146}Nd/^{144}Nd$=0.7219. In addition, USGS reference materials BCR-2 and AGV-2 yielded $^{143}Nd/^{144}Nd$ ratios of 0.512637 ± 5 and 0.512798 ± 5, respectively, which are within analytical uncertainty of their published values (Zhang and Hu, 2020).

4. Results

4.1. Zircon U–Pb ages

Zircon grains from garnet-bearing mafic granulite sample D26-2 are mostly prismatic (200–400 μm) with aspect ratios of 2.0–3.0. In CL images, most zircon grains exhibit core–rim structures that are characterized by oscillatory zoning in the cores and weak luminescence in the rims (Fig. 4a–d), but minor cores are relatively homogeneous. A total of 15 spot analyses were undertaken on 15 zircon cores from this sample. The oscillatory-zoned and homogeneous cores contain variable concentrations of U (20–118 ppm) and Th (15–169 ppm), with relatively high Th/U ratios of 0.77–1.48 (Table 2). Three homogeneous grains (spots 1.1, 6.1, and 10.1) have slightly older $^{206}Pb/^{238}U$ ages of 715–698 Ma (Fig. 5a), and yield a weighted mean $^{206}Pb/^{238}U$ age of 704 ± 10 Ma (MSWD = 1.0). Removing these and one younger datum (spot 7.1), the remaining 11 analyses yield a weighted mean $^{206}Pb/^{238}U$ age of 671 ± 9 Ma (MSWD = 2.0; Fig. 5a).

Zircon grains from mafic granulite sample D31-1 are short to long prismatic in shape, with lengths of 200–500 μm and length-to-width ratios of 2.5–5.0. The majority show typical core–rim structures, composed of banded or weak oscillatory-zoned dark cores and grey overgrowth rims (Fig. 4e–h). A total of 15 spot analyses were carried out on 15 cores in this sample. The zircon cores have U concentrations of 251–720 ppm, Th concentrations of 319–1571 ppm, and Th/U ratios of 1.31–2.07 (Table 2). Three grains (spots 10.1, 13.1, and 14.1) have slightly older $^{206}Pb/^{238}U$ ages of 708–698 Ma (Fig. 5b), and yield a weighted mean $^{206}Pb/^{238}U$ age of 702 ± 13 Ma (MSWD = 1.2). Excluding these and one young data point (spot 3.1), the remaining 11 concordant analyses yield a weighted mean $^{206}Pb/^{238}U$ age of 674 ± 3

Ma (MSWD = 1.3; Fig. 5b).

Zircon grains from mafic granulite sample D34-1 are stubby to prismatic, and occasionally ovoid in shape. Their grain lengths range from 200–400 μm. Most show core–rim structures (Fig. 4i–l). Cores have a relatively low CL response and most exhibit oscillatory bands, although some are homogeneous. The rims are grey and homogeneous in CL images. Fifteen spot analyses were performed on 15 zircon cores from this sample. The zircon cores contain U and Th abundances of 84–459 and 60–714 ppm, respectively, with Th/U ratios of 0.74–1.61 (Table 2). With the exception of one younger datum (spot 7.1), the remaining 14 concordant analyses yield a weighted mean $^{206}Pb/^{238}U$ age of 660 ± 3 Ma (MSWD = 0.5; Fig. 5c).

4.2. Zircon Hf–O isotopes

Zircon Lu–Hf isotope data from the studied metamafic rocks are listed in Table 3. For sample D26-2, 11 Lu–Hf isotope spot analyses were carried out on 11 zircon grains with a weighted mean age of 671 ± 9 Ma, which show rather consistent $^{176}Hf/^{177}Hf$ ratios of 0.28235–0.282398. Initial ε_{Hf} values [$\varepsilon_{Hf}(t)$] calculated at t = 671 Ma vary from −0.3 to +1.5 (Fig. 6), and corresponding Hf depleted mantle model ages [T_{DM}(Hf)] are between 1250 and 1180 Ma. For sample D31-1, 11 Lu–Hf isotope spot analyses on 11 zircon grains with a weighted mean age of 674 ± 3 Ma show coherent $^{176}Hf/^{177}Hf$ ratios of 0.28238–0.282448, $\varepsilon_{Hf}(t)$ values of −0.1 to +2.2 (calculated at t = 674 Ma), and T_{DM}(Hf) ages between 1280 and 1190 Ma. For sample D34-1, 14 Lu–Hf isotope spot analyses on 14 zircon grains with a weighted mean age of 660 ± 3 Ma show $^{176}Hf/^{177}Hf$ ratios of 0.28237–0.282487, $\varepsilon_{Hf}(t)$ values of −0.3 to +3.5 (calculated at 660 Ma), and $T_{DM}(Hf)$ ages between 1260 and 1130 Ma.

The O isotope analyses yield $\delta^{18}O$ values of 2.57 to 4.10‰ with an average of 3.2 ± 0.4‰ for sample D26-2 (Table 4; Fig. 7a), 1.03 to 2.01‰ with an average of 1.6 ± 0.3‰ for sample D31-1 (Table 4; Fig. 7b), and 0.89 to 2.02‰ with an average of 1.4 ± 0.3‰ for sample D34-1 (Table 4; Fig. 7c).

4.3. Major and trace elements

The whole-rock major and trace element compositions for 11 metamafic samples from the Leeuwin Complex are listed in Table 4. The metamafic rocks are basic (SiO_2 = 43.0–52.8 wt%), and have moderate contents of Al_2O_3 (12.2–20.3 wt%), total Fe_2O_3 (10.3–19.0 wt%) and CaO (7.3–10.7 wt%), low contents of MgO (2.0–6.5 wt%), and variable contents of TiO_2 (2.2–5.8 wt%). Their Mg# values (= 100 × Mg/(Mg + Fe^{2+})) range from 22 to 50. In an Nb/Y vs SiO_2 classification diagram (Fig. 8a; Winchester and Floyd, 1977), most samples fall into the field of subalkaline basalt. In an (Na_2O + K_2O)–FeO^T–MgO (AFM) ternary diagram (Irvine and Baragar, 1971), the samples exhibit a tholeiitic trend (Fig. 8b).

In general, the studied metamafic rocks have variable total REE contents of 105–512 ppm (Table 4). They show uniform chondrite-normalized REE patterns with light REE (LREE) enrichment [$(La/Yb)_N$ = 3.55–11.10; $(La/Sm)_N$ = 1.87–3.15] and relatively flat heavy REE (HREE) patterns [$(Dy/Yb)_N$ = 1.23–1.67], which are roughly parallel to the ocean island basalt (OIB) trends (Fig. 9a). In addition, most of the samples do not show distinctive Eu anomalies (δEu (= $2Eu_N/(Gd_N + Sm_N)$) = 0.83–1.37) (Fig. 9a). In a primitive mantle-normalized trace element diagram (Fig. 9b), the metamafic rocks show significant enrichment in Pb, whereas Nb and Ta show small negative anomalies (Nb/Nb* (= $2Nb_{PM}/(Th_{PM} + La_{PM})$) = 0.42–0.96; Fig. 9b), except for one sample (Nb/Nb* = 1.15). Furthermore, 7 of 11 samples exhibit slight negative Ti anomalies (Ti/Ti* (= $2Ti_{PM}/(Sm_{PM} + Tb_{PM})$) = 0.28–0.96; Fig. 9b).

4.4. Whole-rock Sm–Nd isotopes

Whole rock Sm–Nd isotope data of the studied metamafic rocks are listed in Table 5. Initial ε_{Nd} values [$\varepsilon_{Nd}(t)$] and Nd model ages [T_{DM}(Nd)] were calculated at 670 Ma for all samples. The samples have measured $^{143}Nd/^{144}Nd$ ratios ranging from 0.512172 to 0.512437, and $\varepsilon_{Nd}(t)$ values of −1.4 to +1.5, with corresponding T_{DM}(Nd) ages of 1510–1320 Ma.

5. Discussion

5.1. Emplacement ages of the metamafic rocks

The emplacement ages of metamafic rocks in the Leeuwin Complex are poorly constrained (Simons, 2001; Janssen et al., 2003). Zircon cores from all three dated samples are oscillatory-zoned or banded and have relatively high Th/U ratios (>0.70), suggesting a magmatic origin (Rubatto, 2002). Thus, the ages of 674–660 Ma obtained for such zircon domains are interpreted to represent the emplacement ages of the metamafic rocks. Some magmatic zircon cores from samples D26-2 and D31-1 yield slightly older ages of ca.700 Ma that are consistent with the known protolith ages (770–690 Ma) of the country granitic gneisses (Nelson, 1996, 1999, 2002; Collins, 2003; Arnoldi, 2017; our unpublished data). Therefore, we interpret these ages as inherited from the magma sources or incorporated from the wall-rocks. However, considering the similarity of internal structures of zircon from sample D31-1, another possibility that these older ages are resulted from analytical errors cannot be ruled out. In addition, a few younger data points in three samples suggest Pb loss during Cambrian metamorphism.

5.2. Assessment of element mobility

As the rocks from the Leeuwin Complex experienced upper amphibolite- to granulite facies metamorphism (Myers, 1990; Wilde and Murphy, 1990), it is necessary to assess element mobility before discussing their petrogensis. Using the criteria of Polat and Hofman (2003), rocks with loss on ignition (LOI) higher than 6 wt%, or primitive mantle normalized Ce anomalies greater than 1.1 or less than 0.9, are considered to have been variably altered. The analyzed samples show relatively low LOI values of 0.05–0.71 wt%, and primitive mantle normalized Ce/Ce* values of 1.01 to 1.07, indicating that these samples preserve primary chemical signatures (Table 4). In addition, Zr is usually regarded as an alteration-independent index, because it is the least mobile element during post-magmatic alteration and metamorphism (Pearce and Peate, 1995; Polat et al., 2002). For our data, the rare earth elements (REEs), high field strength elements (HFSEs; e.g., Nb, Ta, Ti, Hf, Y), and Th show good linear trends with Zr, indicating that these elements are essentially immobile (Fig. 10). However, some large ion lithophile elements (LILEs; e.g., Rb, Sr) show scatter when plotted against Zr, suggesting mobilization during later alteration and metamorphism (Fig. 10). Consequently, at least immobile elements, including REEs and HSFEs, are used for petrogenetic interpretation.

5.3. Crustal contamination and crystal fractionation

Crustal contamination and crystal fractionation commonly play a crucial role during the ascent and emplacement of mafic magma (Watson, 1982). Typical features of continental crust are depletion in Nb, Ta, and Ti and enrichment in Pb (Rudnick and Gao, 2003). Most of the metamafic rocks from the Leeuwin Complex show small negative anomalies in Nb, Ta, and Ti, and large positive anomalies in Pb (Fig. 7b), indicating an input of continental crust components. Moreover, previous studies have indicated that the $(Th/Ta)_{PM}$ and $(La/Nb)_{PM}$ values of basalts derived from mantle plumes are both <1, and the $(Th/Ta)_{PM}$–$(La/Nb)_{PM}$ diagram can elucidate the contribution of continental crust (Frey et al., 2002; Neal et al., 2002; Zhu et al., 2006). In this diagram (Fig. 11a), all of the studied samples plot outside of the mantle plume basalt field and show good correspondence with sialic crust, which is also supported in diagrams of Th/La vs Nb/Th, Th/La vs Nb/La, and La/Sm vs $\varepsilon_{Nd}(t)$ (Fig. 11b–d). Collectively, these observations confirm that the primary magma of the metamafic rocks was contaminated by continental crust.

Crustal contamination is generally accompanied by fractional crystallization during the emplacement of primary magmas. It is commonly considered that primary mantle-derived magmas contain high contents of Ni (>400 ppm) and Cr (>1000 ppm; Wilson, 1989), and high Mg# values (>73; Sharma, 1997). However, metamafic rocks from the Leeuwin Complex exhibit lower Mg# (22–50), Ni (<115 ppm), and Cr (<105 ppm) relative to these primary magmas, indicating that they underwent fractional crystallization to varying degrees. In general, the SiO_2, Na_2O, K_2O, and P_2O_5 contents of the rocks show a negative correlation with increasing MgO (Fig. 12a, b, c), whereas $Fe_2O_3^T$, TiO_2, Cr, and Ni concentrations show a positive correlation againist MgO (Fig. 12d, e, f, g). The negative correlation between P_2O_5 and MgO suggests that apatite fractionation was likely suppressed (Fig. 12c). In contrast, the positive correlation between $Fe_2O_3^T$ and TiO_2 with MgO indicates fractionation of Fe–Ti oxides (Fig. 12d, e). The positive correlations are shown in MgO-variation Harker diagrams with Ni and Cr (Fig. 12f, g), indicating that they might have experienced some degree of fractionation of clinopyroxene and/or minor olivine. Moreover, the positive correlation between CaO/Al_2O_3 and MgO suggests fractionation of clinopyroxene (Fig. 12h) but no significant fractionation of plagiocalse, as supported by indistinctive Eu anomalies.

5.4. Nature of mantle source and melting conditions

In general, the ratios of incompatible elements and Nd and Hf isotopic compositions are considered insensitive to partial melting and fractionation crystallization processes, and can be used to evaluate the nature of the mantle source (Weaver, 1991). Although the parental magma experienced crustal contamination, some metamafic samples have positive $\varepsilon_{Nd}(t)$ (up to +1.5) and zircon $\varepsilon_{Hf}(t)$ (up to +3.5) values, indicating that the parental magma was originated from a relatively depleted mantle source. Both the REE and other trace element patterns of the metamafic rocks are roughly parallel to OIB trends (Fig. 7). In a Ti–Sm–V ternary diagram, all of the samples plot within the OIB field (Fig. 13a). However, continental crust is characterized by depletion in Nb and enrichment in Ta and Th, Zr, Hf, and LREEs, and crustal contamination process can lead to a decrease in Ta/La and Nb/La ratios (Rudnick and Gao, 2003). The studied samples deviate slightly from the OIB field, but are clearly distinct from subduction-related rocks, as shown in a $(Ta/La)_{PM}$ vs $(Hf/Sm)_{PM}$ diagram (Fig. 13b). In addition, low Nb/La ratios mean these samples plot in the mixed asthenospheric mantle field in a La/Yb vs Nb/La diagram (Fig. 13c). Consequently, the studied metamafic rocks possibly formed by melting of asthenosphere and were contaminated by continental crust during ascent. This mechanism may explain the OIB-like trace element patterns with depletion in Nb and Ta (Fig. 7b), as well as the slightly enriched Nd and Hf isotopic compositions.

Both REE variations and incompatible element ratios are effective tools for evaluating the conditions of mantle melting in typical mantle phases (Aldanmaz et al., 2000). In a Sm vs Sm/Yb diagram (Fig. 13d), the majority of the studied samples plot at compositions consistent with formation near the spinel–garnet transition within a mixed lherzolite mantle source, indicating that the parental magma was derived from depths of 60–80 km (Pouclet et al., 1994). In addition, the source is suggested to have experienced a relatively low degree of partial melting (1–10%; Fig. 13d).

5.5. Tectonic setting

As mentioned previously, metamafic rocks from the Leeuwin Complex are characterized by variable TiO_2 contents and enrichment in LREEs, and most exhibit small negative Nb and Ta anomalies. These general geochemical features are typically interpreted to be associated with either subduction-related volcanic arc magmas (e.g. Pearce, 1982; Keppler, 1996; You et al., 1996) or contaminated continental basaltic magmas (e.g. Xia et al., 2007, 2009a; Xia, 2014). However, in detail, these two tectonic settings differ in their geochemical features (Xia, 2014), as follows. (1) The overall incompatible element concentrations of contaminated continental basalts, including Nb contents, are higher than in subduction-related volcanic arc basalts, and the former commonly have relatively low $\varepsilon_{Nd}(t)$ values. (2) In tectonic discrimination diagrams that do not include Nb, Ta, or Ti, contaminated continental basalts show a within-plate affinity. The studied metamafic rocks have much higher Nb contents (13.2–56.4 ppm) than those of subduction-related volcanic arc basalts (<4 ppm; Tatsumi and Eggins, 1995), and relatively low $\varepsilon_{Nd}(t)$ values (−1.4 to +1.5), consistent with a continental affinity. In addition, the impact of crustal contamination on Zr and Y contents is negligible, such that tectonic discrimination diagrams that involve Zr and Y are effective in distinguishing these two tectonic settings (Xia et al., 2007, 2009a; Xia, 2014). In a Zr vs Zr/Y diagram, all studied samples plot close to the field of within-plate basalt (Fig. 14a; Pearce and Norry, 1979), and this conclusion is also supported by other different tectonic discrimination diagrams (Fig. 14b–d; Cabanis and Lecolle, 1989; Gorton and Schandl, 2000; Wang et al., 2001). Furthermore, slightly older (770–690 Ma; our unpublished data) felsic intrusive rocks in the Leeuwin Complex have geochemical affinities with A-type granites, consistent with a continental rift setting (Wilde and Murphy, 1990; Wilde, 1999; Collins and Fitzsimons, 2001; Collins, 2003). From a broader perspective, some Neoproterozoic (ca. 750 Ma) rift-related mafic intrusive rocks have been identified in the northern Pinjarra Orogen (Wingate and Giddings, 2000; Janssen et al., 2003; Li et al., 2006), consistent with continuous lithospheric extension along the western margin of Western Australia during the Neoproterozoic. In the wider tectonic contexts, this region was commonly placed in the edge of Rodinia (Powell and Pisarevsky, 2002; Collins and Pisarevsky, 2005; Li et al., 2008; Merdith et al., 2017, 2021), and the extension and rifting of the region in the Neoproterozoic were thought to have resulted from the Rodinia breakup.

5.6. Genesis of the low-δ^{18}O mafic magma

It is generally thought that zircon preserves primary oxygen isotopic compositions, even when it has undergone sub-solidus crystallization during granulite facies metamorphism (Chemiak and Watson, 2003; Zheng et al., 2004). However, in some cases, post-magmatic processes, such as metamorphic recrystallization and grain-scale diffusion, can modify the primary oxygen isotopic compositions (Hoskin, 2005; Geisler et al., 2007). Magmatic zircon might experience solid-state transformation, dissolution–reprecipitation, and/or metasomatic alteration (Xia et al., 2009b, 2010; Chen et al., 2010, 2011). Solid-state transformation may result in radiogenic Pb loss in zircon, and younger apparent U–Pb ages, although $\delta^{18}O$ may not be affected (e.g. Chemiak and Watson, 2003; Zheng et al., 2004). Fluid components can enter recrystallized domains in zircon during dissolution–reprecipitation, resetting the U–Pb radiometric system and oxygen isotopic compositions (e.g. Geisler et al., 2007; Xia et al., 2010; Chen et al., 2010, 2011). Metasomatic alteration commonly resets the isotopic compositions of zircon grains along cracks and grain boundaries (e.g. Chen et al., 2010, 2011; Xia et al., 2013; Gao et al., 2015).

The $\delta^{18}O$ values of analyzed zircon grains from three samples range from 0.89 to 4.10‰, which are lower than those of normal mantle zircon (5.3 ± 0.3‰; Valley et al., 1998). The dated zircon cores show features typical of a magmatic origin. Although most zircon grains have a thin overgrowth that grew during Cambrian upper amphibolite- to granulite-facies metamorphism, the primary internal structures of zircon cores are well preserved except the appearance of a few patches and microscopic fractures in some cores. Therefore, the effect of solid-state transformation by later metamorphism may be negligible. Furthermore, except for a few inherited grains, magmatic zircon domains yield mostly concordant ages clustered between 674 and 660 Ma. In this regard, dissolution–reprecipitation and/or metasomatic alteration as well as the effect of metamictization can be ruled out as these three mechanisms would reset the U–Pb radiometric system. Coupled with the relatively narrow range of $\delta^{18}O$ values for each sample, we conclude that the low-$\delta^{18}O$

values of metamafic rocks from the Leeuwin Complex may represent the primary isotopic compositions of their protoliths.

As most low-$\delta^{18}O$ magmatic rocks on Earth are felsic in composition, previous studies have focused mainly on low-$\delta^{18}O$ felsic rocks. In general, supracrustal rocks are more likely to exchange oxygen with low-$\delta^{18}O$ natural reservoirs at high temperature, producing low-$\delta^{18}O$ felsic rocks (Valley et al., 1998, 2005; Troch et al., 2020). There are also some occurrences of low-$\delta^{18}O$ mafic rocks, such as Iceland basalts and sporadic Neoproterozoic mafic intrusive rocks from the northern margin of the South China Block (Zheng et al., 2003, 2006, 2008; Pope et al., 2013; Li and Zhao, 2016; Wu, 2019). However, the genesis of low-$\delta^{18}O$ zircon from mafic rocks is more complicated. Based on low-$\delta^{18}O$ eclogites and granitic gneisses from the Dabie–Sulu orogenic belt in central China, Zheng et al. (2003) proposed two possible formation mechanisms for low-$\delta^{18}O$ zircon in mafic rocks: (1) direct oxygen isotope exchange between mafic rocks and low-$\delta^{18}O$ fluid at high temperature; and (2) partial melting of pre-existing low-$\delta^{18}O$ hydrothermally altered mafic rocks. However, low-$\delta^{18}O$ hypabyssal mafic intrusive rocks can also be interpreted as a consequence of contamination of mantle-derived mafic magmas by low-$\delta^{18}O$ hydrothermally-altered crust (Zheng et al., 2003; Wang and Eiler, 2008; Genske et al., 2013; Seligman et al., 2014; Li and Zhao, 2016; Zhao et al., 2018; Zakharov et al., 2019; Li et al., 2020).

As mentioned previously, the host rocks of the metamafic rocks in the Leeuwin Complex are 770–690 Ma A-type metagranitoids that formed in a continental rift setting. Zircon from these orthogneisses also yielded low $\delta^{18}O$ values ranging from

1.32 to 4.80‰ (in average for each of 7 samples; our unpublished data). Geochemical data indicate that the protoliths of the metamafic rocks were contaminated by the host rocks, which can result in low $\delta^{18}O$ values within the metamafic rocks. Modeling calculations from zircon Hf–O isotopic data reveal that the $\delta^{18}O$ values (0.89–4.10‰) of the metamafic rocks would require 20–80% low-$\delta^{18}O$ felsic crustal material inputs if considering only crustal contamination (Fig. 15). However, excessive crustal contributions would lead to a significant deviation from mafic compositions, which are inconsistent with our whole-rock geochemical data. The field observations of the metamafic rocks suggest that their protoliths were mafic dykes intruded at relatively shallow levels (Fig. 3a–c). Therefore, direct oxygen isotope exchange between mafic magma and low-$\delta^{18}O$ fluid at shallow depths can also occur and might have played an important role in the formation of the low-$\delta^{18}O$ metamafic rocks.

Based on the above analysis, we propose an integrated tectonic model to explain the petrogenesis of low-$\delta^{18}O$ metamafic rocks from the Leeuwin Complex (Fig. 16). Continuous lithospheric extension during the period 770–690 Ma occurred concomitantly with high crustal permeability and high thermal gradients, which greatly expand the field of high temperature hydrothermal alteration to depths of 10–15 km (Zheng et al., 2004, 2007a; Zhang and Zheng, 2011; Troch et al., 2020). These processes can facilitate high temperature hydrothermal alteration in the middle- to lower continental crust (Li et al., 2020), resulting in the generation of low-$\delta^{18}O$ A-type felsic rocks. Subsequently, the parental mafic magmas, which originated from upwelling asthenosphere, were contaminated by low-$\delta^{18}O$ felsic crustal wall rocks. As the magma moved to shallow depths, it would have interacted with low-$\delta^{18}O$ surface water at relatively high temperature. Finally, the low-$\delta^{18}O$ mafic magmas were emplaced at 674–660 Ma in response to widespread rift-related magmatism during the Neoproterozoic (820–620 Ma) (Li et al., 2003; Zheng et al., 2004).

6. Conclusions

Our integrated geochronological, geochemical, and isotopic study of metamafic rocks from the Leeuwin Complex leads to the following conclusions.

(1) The protoliths of the metamafic rocks in the Leeuwin Complex were emplaced at 674–660 Ma, slightly later than the intrusion of voluminous felsic magmas.

(2) The metamafic rocks have OIB-like tholeiitic affinities. They originated from a depleted asthenospheric mantle source that experienced relatively low-degree partial melting. The parental magma underwent a degree of crustal contamination and fractional crystallization during its emplacement.

(3) The low-$\delta^{18}O$ zircon (0.89–4.10‰) within the metamafic rocks records the primary and magmatic oxygen isotopic compositions. These low-$\delta^{18}O$ metamafic rocks were generated by contamination with low-$\delta^{18}O$ felsic crustal wall rocks and interaction of the magmas with surface water at shallow depths.

Acknowledgements

We appreciate the kind assistance of Juan Hu, Guanggao Zheng, and Mengmeng Xia with SHRIMP U–Pb dating and for fruitful discussions. Yinglei Li, Qiqi Zhang, and Tan Shu are also thanked for their kind assistance with software operation and data analysis. Critical reviews by Alan Collins and an anonymous reviewer substantially improved the manuscript. This research was funded by the National Natural Science Foundation of China (41941004, 41530209, and 41802064), the Fundamental Research Funds of the Chinese Academy of Geological Sciences (JYYWF201819 and DZLXJK202003), and the Geological Investigation Project of the Chinese Geological Survey (DD20190579).

References

Aldanmaz, E., Pearce, J.A., Thirlwall, M.F., Mitchell, J.G., 2000. Petrogenetic evolution of late Cenozoic, post-collision volcanism in western Anatolia, Turkey. J. Volcanol. Geoth. Res. 102, 67–95.

Archibald, D.B., Collins, A.S., Foden, J.D., Payne, J.L., Holden, P., Razakamanana, T., De Waele, B., Thomas, R.J., Pitfield, P.E.J., 2016. Genesis of the Tonian Imorona-Itsindro magmatic Suite in central Madagascar: Insights from U–Pb, oxygen and hafnium isotopes in zircon. Precambrian Res. 281, 312–337.

Arnoldi, S., 2017. Spatial and temporal relationships in rocks of the Leeuwin Complex, and their setting within the Pinjarra Orogen of the Western Australia. B. Sc. thesis, Curtin University of Technology, Perth.

Balsley, S.D., Gregory, R.T., 1998. Low-^{18}O silicic magmas: why are they so rare? Earth Planet. Sci. Lett. 162, 123–136.

Bindeman, I.N., 2008. Oxygen isotopes in mantle and crustal magmas as revealed by

single crystal analysis. Rev. Mineral. Geochem. 69, 445–478.
Bindeman, I.N., Ponomareva, V.V., Bailey, J.C., Valley, J.W., 2004. Volcanic arc of Kamchatka: a province with high-$\delta^{18}O$ magma sources and large-scale $^{18}O/^{16}O$ depletion of the upper crust. Geochim. Cosmochim. Acta 68:841–865.
Bindeman, I.N., Serebryakov, N.S., 2011. Geology, petrology and O and H isotope geochemistry of remarkably ^{18}O depleted Paleoproterozoic rocks of the Belomorian Belt, Karelia, Russia, attributed to global glaciation 2.4 Ga. Earth Planet. Sci. Lett. 306, 163–174.
Bindeman, I.N., Valley, J.W., 2001. Low-$\delta^{18}O$ rhyolites from Yellowstone: Magmatic evolution based on analyses of zircons and individual phenocrysts. J. Petrol. 42, 1491–1517.
Black, L.P., Kamo, S.L., Allen, C.M., Aleinikoff, J.N., Davis, D.W., Korsch, R.J., Foudoulis, C., 2003. TEMORA 1: a new standard for Phanerozoic U–Pb geochronology. Chem. Geol. 200, 155–170.
Bodorkos, S., Fitzsimons, I.C.W., Hall, L., Sircombe, K., Lewis, C.J., 2016. Beneath the Perth Basin: New U–Pb SHRIMP zircon ages from the Pinjarra Orogen, Western Australia. Geoscience Australia, Canberra.
Cabanis, B., Lecolle, M., 1989. Le diagramme La/10–Y/15–Nb/8: Un outil pour la discrimination des séries volcaniques et la mise en évidence des processus de mélange 682 et/ou de contamination crustale. Compt. Rendus Acad. Sci. Ser. II 309, 2023–2029.
Cawood, P.A., Korsch, R.J., 2008. Assembling Australia: Proterozoic building of a

continent. Precambrian Res. 166, 1–35.

Chen, R.X., Zheng, Y.-F., Xie, L., 2010. Metamorphic growth and recrystallization of zircon: Distinction by simultaneous in-situ analyses of trace elements, U–Th–Pb and Lu–Hf isotopes in zircons from eclogite-facies rocks in the Sulu orogen. Lithos 114, 132–154.

Chen, Y.X., Zheng, Y.F., Chen, R.X., Zhang, S.B., Li, Q., Dai, M., Chen, L., 2011. Metamorphic growth and recrystallization of zircons in extremely ^{18}O-depleted rocks during eclogite-facies metamorphism: evidence from U–Pb ages, trace elements, and O–Hf isotopes. Geochim. Cosmochim. Acta 75, 4877–4898.

Cherniak, D.J., Watson, E.B., 2003. Diffusion in zircon. Rev. Miner. Geochem. 53, 113–143.

Collins, A.S., 2003. Structure and age of the northern Leeuwin Complex, Western Australia: constraints from field mapping and U–Pb isotopic analysis. Australian J. Earth Sci. 50, 585–599.

Collins, A.S., Fitzsimons, I.C.W., 2001. Structural, isotopic and geochemical constraints on the evolution of the Leeuwin Complex, SW Australia. From basins to mountains: Rodinia at the turn of the century. Geological Society of Australia, Perth, 65, 16–19.

Collins, A.S., Pisarevsky, S.A., 2005. Amalgamating eastern Gondwana: The evolution of the Circum-Indian Orogens. Earth-Sci. Rev. 71, 229–270

Dobosi, G., Kempton, P.D., Downes, H., Embey-Isztin, A., Thirlwall, M., Greenwood, P., 2003. Lower crustal granulite xenoliths from the Pannonian Basin, Hungary, Part 2: Sr–Nd–Pb–Hf and O isotope evidence for formation of continental lower crust by tectonic emplacement of oceanic crust. Contrib. Mineral. Petrol. 144, 671–683.

Fisher, C.M., Hanchar, J.M., Samson, S.D., Dhuime, B., Blichert-Toft, J., Vervoort, J.D., Lam, R., 2011. Synthetic zircon doped with hafnium and rare earth elements: a reference material for in situ hafnium isotope analysis. Chem. Geol. 286, 32–47.

Fu, B., Brocker, M., Ireland, T., Holden, P., Kinsley, L.P.J., 2015. Zircon U–Pb, O, and Hf isotopic constraints on Mesozoic magmatism in the Cyclades, Aegean Sea. Greece. Int. J. Earth Sci. 104, 75–87.

Fu, B., Kita, N.T., Wilde, S.A., Liu, X.C., Cliff, J., Greig, A., 2013. Origin of the Tongbai-Dabie-Sulu Neoproterozoic low-$\delta^{18}O$ igneous province, east-central China. Contrib. Mineral. Petrol. 165, 641–662.

Gao, X.Y., Zheng, Y.F., Chen, Y.X., Tang, H.L., Li, W.C., 2015. Zircon geochemistry records the action of metamorphic fluid on the formation of ultrahigh-pressure jadeite quartzite in the Dabie orogen. Chem. Geol. 419, 158–175.

Geisler, T., Schaltegger, U., Tomaschek, F., 2007. Re-equilibration of Zircon in Aqueous Fluids and Melts. Elements 3, 43–50.

Genske, F.S., Beier, C., Haase, K.M., Turner, S.P., Krumm, S., Brandl, P.A., 2013. Oxygen isotopes in the Azores islands: crustal assimilation recorded in olivine. Geology 41, 491–494.

Gorton, M.P., Schandl, E.S., 2000. From continents to island arcs: a geochemical index of tectonic setting for arc-related and within-plate felsic to intermediate volcanic rocks. The Can. Mineral. 38, 1065–1073.

Harris, C., Ashwal, L.D., 2002. The origin of low-δ^{18}O granites and related rocks from the Seychelles. Contrib. Mineral. Petrol. 143, 366–376.

He. Q., Zhang. S.B., Zheng. Y.F., 2016. High temperature glacial meltwater–rock reaction in the Neoproterozoic: Evidence from zircon in-situ oxygen isotopes in granitic gneiss from the Sulu orogeny. Precambrian Res. 284, 1–13.

Hiess, J., Bennett, V.C., Nutman, A.P., Williams, I.S., 2009. In situ U–Pb, O and Hf isotopic compositions of zircon and olivine from Eoarchaean rocks, West Greenland: new insights to making old crust. Geochim. Cosmochim. Acta 73, 4489–4516.

Hoefs, J., 2009. Stable Isotope Geochemistry, 6th ed. Springer-Verlag, Berlin Heidelburg.

Hoskin, P.W.O., 2005. Trace-element composition of hydrothermal zircon and the alteration of Hadean zircon from the Jack Hills. Australia. Geochim. Cosmochim. Acta 69, 637–648.

Ickert, R.B., Hiess, J., Williams, I.S., Holden, P., Ireland, T.R., Lanc, P., Schram, N., Foster, J.J., Clement, S.W., 2008. Determining high precision, in situ, oxygen isotope ratios with a SHRIMP II: analyses of MPI-DING silicate-glass reference materials and zircon from contrasting granites. Chem. Geol. 257, 114–128.

Irvine, T., Baragar, W., 1971. A guide to the chemical classification of the common volcanic rocks. Can. J. Earth Sci. 8, 523–548.

Janssen, D.P., Collins, A.S., Fitzsimons, I.C.W., 2003. Structure and tectonics of the Leeuwin Complex and Darling Fault Zone, southern Pinjarra Orogen, Western Australia–a field guide. Geological Survey of Western Australia, Perth.

Janssen, D.P., Fitzsimons, I.C.W., 2005. The Leeuwin Complex: Proterozoic terrane assembly along Australia's western margin. Gondwana 12: Geological and Biological Heritage of Gondwana, Cordoba, p. 212.

Janssen, D.P., Fitzsimons, I.C.W., Collins, A.S., 2004. The Leeuwin Complex, Southwest Australia: disparate blocks amalgamated at ~550 Ma? 17th Australian Geological Convention, Hobart, p. 167.

Kelemen, P.B., Hanghj, K., Greene, A.R., 2007. One view of the geochemistry of subduction-related magmatic arcs, with an emphasis on primitive andesite and lower crust. Treatise on Geochemistry, 3, 1–70.

Keppler, H., 1996. Constraints from partitioning experiments on the composition of subduction_zone fluids. Nature 380, 237–240.

La Flèche, M.R., Camire, G., Jenner, G.A., 1998. Geochemistry of post-Acadian, Carboniferous continental intraplate basalts from the Maritimes Basin, Magdalen islands, Quebec, Canada. Chem. Geol. 148, 115–136.

Li, Q.W., Zhao, J.H., 2016. Petrogenesis of the Wudang mafic dikes: Implications of changing tectonic settings in South China during the Neoproterozoic. Precambrian Res. 272, 101–114.

Li, X.H., Li, Z.X., Wingate, M.T.D., Chung, S.L., Liu, Y., Lin, G.C., Li. W.X., 2006. Geochemistry of the 755 Ma Mundine Well dyke swarm, northwestern Australia:

part of a Neoproterozoic mantle superplume beneath Rodinia? Precambrian Res. 146, 1–15.

Li, X.H., Zeng, Z.G., Dan, W., Yang, H.X., Wang, X.Y., Fang, B.W., Li, Q.L., 2020. Source lithology and crustal assimilation recorded in low-$\delta^{18}O$ olivine from Okinawa Trough, back-arc basin. Lithos 360–361, 105444.

Li, Z.X., Li, X.H., Kinny, P.D., Wang, J., Zhang, S., Zhou, H., 2003. Geochronology of Neoproterozoic syn-rift magmatism in the Yangtze Craton, South China and correlations with other continents: evidence for a mantle superplume that broke up Rodinia. Precambrian Res. 122, 85–109.

Li, Z.X., Bogdanova, S.V., Collins, A.S., Davidson, A., De Waele, B., Ernst, R.E., Fitzsimons, I.C.W., Fuck, R.A., Gladkochub, D.P., Jacobs, J., Karlstron, K.E., Lu, S., Natapov, L.M., Pease, V., Pisarevsky, S.A., Thrane, K., Vernikovsky, V., 2008. Assembly, configuration, and break-up history of Rodinia: a synthesis. Precambrian Res. 160, 179–210.

Lin, J., Liu, Y.S., Yang, Y.H., Hu, Z.C., 2016. Calibration and correction of LA–ICP–MS and LA–MC–ICP–MS analyses for element contents and isotopic ratios. Solid Earth Sci. 1, 5–27.

Liu, J. B., Zhang, L. M., 2013. Neoproterozoic low to negative $\delta^{18}O$ volcanic and intrusive rocks in the Qinling Mountains and their geological significance. Precambrian Res. 230, 138–167.

Liu, J. B., Zhang, L. M., Ye, K., Su, W., Cheng, N. F., 2013. Oxygen isotopes of whole-rock and zircon and zircon U−Pb ages of meta-rhyolite from the

Luzhenguan group and associated meta-granite in the northern Dabie Mountains. Acta. Petrolo. Sinica 29, 1511–1524 (in Chinese with English Abstract).

Ludwig, K.R., 2001. SQUID 1.02: a user’s manual. Berkeley Geochronology Center. Special Publication, No. 2.

Ludwig, K.R., 2003. User’s manual for Isoplot 3.00. A geochronological Toolkit for Microsoft Excel. Berkeley Geochronology Center. Special Publication, No. 4a.

Mcdonough, W.F., 1990. Constraints on the composition of the continental lithospheric mantle. Earth Planet. Sci. Lett. 101, 1–18.

Merdith, A.S., Collins, A.S., Williams, S.E., Pisarevsky, S., Foden, J.D., Archibald, D.B., Blades, M.L., Alessio, B.L., Armistead, S., Plavsa, D., Clark, C., Muller, R.D., 2017. A full-plate global reconstruction of the Neoproterozoic. Gondwana Res. 50, 84–134.

Merdith, A.S., Williams, S.E., Collins, A.S., Tetley, M.G., Mulder, J.A., Blades, M.L., Young, A., Armistead, S.E., Cannon, J., Zahirovic, S., Müller, R.D., 2021. Extending full-plate tectonic models into deep time: Linking the Neoproterozoic and the Phanerozoic. Earth-Sci. Rev. 214, 103477.

Myers, J.S., 1990. Pinjarra Orogen. In: Geology and mineral resources of Western Australia. Geological Survey of Western Australia, Perth, pp. 265–274.

Neal, C.R., Mahoney, J.J., Chazey, W.J., 2002. Mantle sources and the highly variable role of continental lithosphere in basalt petrogenesis of the Kerguelen Plateau and Broken Ridge LIP: results from ODP Leg 183. J. Petrol. 43, 1177–1205.

Nelson, D.R., 1996. Compilation of SHRIMP U–Pb zircon geochronology data, 1995.

Geological Survey of Western Australia, Perth.

Nelson, D.R., 1999. Compilation of SHRIMP U–Pb zircon geochronology data, 1998. Geological Survey of Western Australia, Perth.

Nelson, D.R., 2002. Compilation of geochronological data, 2001. Geological Survey of Western Australia, Perth.

Nowell, G.M., Kempton, P.D., Noble, S.R., Fitton, J.G., Saunders, A.D., Mahoney, J.J., Taylor, R. N., 1998. High precision Hf isotope measurements of MORB and OIB by thermal ionization mass spectrometry: insights into the depleted mantle. Chem. Geol. 149, 211–233.

Pearce, J.A., 1982. Trace element characteristics of lavas from destructive plate boundaries. In: Thorps, R.S. (Ed.), Andesites. John Wiley and Sons, New York, pp. 525–548.

Pearce, J.A., Norry, M.J., 1979. Petrogenetic implications of Ti, Zr, Y, and Nb variations in volcanic rocks. Contrib. Mineral. Petrol. 69, 33–47.

Pearce, J.A., Peate, D.W., 1995. Tectonic implications of the composition of volcanic ARC magmas. Annu. Rev. Earth Planet. Sci. 23, 251–285.

Polat, A., Hofmann, A.W., 2003. Alteration and geochemical patterns in the 3.7–3.8 Ga Isua greenstone belt, West Greenland. Precambrian Res. 126, 197–218.

Polat, A., Hofmann, A.W., Rosing, M.T., 2002. Boninite-like volcanic rocks in the 3.7–3.8 Ga Isua greenstone belt, West Greenland: geochemical evidence for intraoceanic subduction zone processes in the early Earth. Chem. Geol. 184, 231–254.

Pope, E.C., Bird, D.K., Arnórsson, S., 2013. Evolution of low-^{18}O Icelandic crust. Earth Planet. Sci. Lett. 374, 47–59.

Pouclet, A., Lee, J.S., Vidal, P., Cousens, B., Bellon, H., 1994. Cretaceous to Cenozoic volcanism in South Korea and in the Sea of Japan: magmatic constraints on the opening of the back-arc basin. Geol. Soc. Lond. Spec. Publ. 81, 169–191.

Powell, C.M., Pisarevsky, S.A., 2002. Late Neoproterozoic assembly of East Gondwana. Geology 30, 3–6.

Rubatto, D., 2002. Zircon trace element geochemistry: partitioning with garnet and the link between U–Pb ages and metamorphism. Chem. Geol. 184, 123–138.

Rudnick, R.L., Gao, S., 2003. 3.01-composition of the continental crust. Treatise Geochem. 1, 1–64.

Seligman, A., Bindeman, I., Jicha, B., Ellis, B., Ponomareva, V., Leonov, V., 2014. Multi-cyclic and isotopically diverse silicic magma generation in an arc volcano: Gorely Eruptive Center, Kamchatka, Russia. J. Petrol. 55, 1561–1594.

Sharma, M., 1997. Siberian traps. In: Mahoney, J.J., Coffin, M.F. (Eds.), Large Igneous Provinces: Continental, Oceanic, and Planetary Flood Volcanism, vol. 100. American Geophysical Union Geophysical Monograph, pp. 273–295.

Simons, S.L., 2001. Nature and origin of the mafic dykes within the late Proterozoic Leeuwin Complex, Western Australia. B. Sc. thesis, Curtin University of Technology, Perth.

Sláma, J., Kǒsler, J., Condon, D.J., Crowley, J.L., Gerdes, A., Hanchar, J.M., Horstwood, M.S.A., Morris, G.A., Nasdala, L., Norberg, N., Schaltegger, U., Schoene, B., Tubrett, M.N., Whitehouse, M.J., 2008. Plesovice zircon–A new natural reference material for U-Pb and Hf isotopic microanalysis. Chem. Geol. 249, 1–35.

Sun, S.S., McDonough, W.F., 1989. Chemical and isotopic systematics of oceanic basalts: implications for mantle composition and processes. Geological Society, London, Special Publications 42, 313-345.

Tatsumi, Y., Eggins, S.M., 1995. Subduction zone magmatism. Blackwell Science, Cambridge, pp. 211.

Troch, J., Ellis, B.S., Harris, C., Bachmann, O., Bindeman, I.N., 2020. Low-δ^{18}O silicic magmas on earth: a review. Earth Sci. Rev. 208, 103299.

Valley, J.W., Kinny, P.D., Schulze, D.J., Spicuzza, M.J., 1998. Zircon megacrysts from kimberlite: oxygen isotope variability among mantle melts. Contrib. Mineral. Petrol. 133, 1–11.

Valley, J.W., Lackey, J.S., Cavosie, A.J., Clechenko, C.C., Spicuzza, M.J., Basei, M.A.S., Bindeman, I.N., Ferreira, V.P., Sial, A.N., King, E.M., Peck, W.H., Sinha, A.K., Wei, C.S., 2005. 4.4 billion years of crustal maturation: oxygen isotope ratios of magmatic zircon. Contrib. Mineral. Petrol. 150, 561–580.

Vermeesch, P., 2006. Tectonic discrimination diagrams revisited. Geochem. Geophys. Geosyst. 7, 466–480.

Wang, L., He, H.L., Li, B., 2003. Multi-element determination in geological samples by Inductively Coupled Plasma Mass Spectrometry after fusion-precipitation treatment. Rock and Mineral Analysis. 22, pp. 86–92 (in Chinese with English abstract).

Wang, W., Cawood, P.A., Zhou, M.F., Pandit, M.K., Xia, X.P., Zhao, J.H., 2017. Low-$\delta^{18}O$ Rhyolites From the Malani Igneous Suite: A Positive Test for South China and NW India Linkage in Rodinia. Geophys. Res. Lett. 40, 10298–10305.

Wang, Y., Zhang, C., Xiu, S., 2001. Th/Hf–Ta/Hf identification of tectonic setting of basalts. Acta Petrol. Sin. 17, 413–421 (in Chinese with English abstract).

Wang, Z., Eiler, J.M., 2008. Insights into the origin of low-$\delta^{18}O$ basaltic magmas in Hawaii revealed from in situ measurements of oxygen isotope compositions of olivines. Earth Planet. Sci. Lett. 269, 377–387.

Watson, S., 1993. Rare earth element inversions and percolation models for Hawaii. J. Petrol. 34, 763–783.

Watson, E.B., 1982. Basalt contamination by continental crust: some experiments and models. Contrib. Miner. Petrol. 80, 73–87.

Weaver, B.L., 1991. The origin of ocean island basalt end-member compositions: trace element and isotopic constraints. Earth Planet. Sci. Lett. 104, 381–397.

Wilde, S.A., 1999. Evolution of the western margin of Australia during the Rodinian and Gondwanan supercontinent cycles. Gondwana Res. 2, 481–499.

Wilde, S.A., Murphy, D.M.K., 1990. The nature and origin of late Proterozoic high-grade gneisses of the Leeuwin Block, Western Australia. Precambrian Res. 47, 251–270.

Williams, I.S., 1998. U–Th–Pb geochronology by ion microprobe. In: McKibben, M.A., Shanks, W.C., Ridley, W.I. (Eds.), Applications of Microanalytical Techniques to Understanding Mineralizing Processes, Reviews in Economic Geology, 7, pp. 1–35.

Wilson, M., 1989. Igneous Petrogenesis. Chapman & Hall, London, pp. 466.

Winchester, J.A., Floyd, P.A., 1977. Geochemical discrimination of different magma series and their differentiation products using immobile elements. Chem. Geol. 20, 325–343.

Wingate, M.T.D., Giddings, J.W., 2000. Age and palaeomagnetism of the Mundine Well dyke swarm, western Australia: implications for an Australia–Laurentia connection at 755 Ma. Precambrian Res. 100, 335–357.

Woodhead, J.D., Hergt, J.M., 2005. A Preliminary appraisal of seven natural zircon reference materials for in situ Hf isotope determination. Geostand. Geoanal. Res. 29, 183–195.

Woodhead, J., Hergt, J.M., Shelley, M., Eggins, S., Kemp, R., 2004. Zircon Hf-isotope analysis with an excimer laser, depth profling, ablation of complex geometries, and concomitant age estimation. Chem. Geol. 209, 121–135.

Wu, P., 2019. Geochemical study of the Neoproterozoic igneous rocks from the northwestern margin of the South China Block. PhD. thesis, University of Science and Technology of China, Hefei.

Wu. P., Zhang. S.B., Zheng. Y.F., Li. Q.L., Li. Z.X., Sun. F.Y., 2020. The occurrence of Neoproterozoic low $\delta^{18}O$ igneous rocks in the northwestern margin of the South China Block: Implications for the Rodinia configuration. Precambrian Res.

347, 105841.

Xia, L.Q., 2014. The geochemical criteria to distinguish continental basalts from arc related ones. Earth Sci. Rev. 139, 195–212.

Xia, L.Q., Xia, Z.C., Xu, X.Y., Li, X.M., Ma, Z.P., 2007. The discrimination between continental basalt and island arc basalt based on geochemical method. Acta Petrol. et Mineral. 26, 77–89 (in Chinese with English abstract).

Xia, L.Q., Xia, Z.C., Xu, X.Y., Li, X.M., Ma, Z.P., 2009a. Do the Tianshan Carboniferous volcanic successions contain Nb-enriched arc basalts? Earth Sci. Front. 16, 303–317 (in Chinese with English abstract).

Xia, Q.X., Zheng, Y.F., Chen, Y.X., 2013. Protolith control on fluid availability for zircon growth during continental subduction-zone metamorphism in the Dabie orogen. J. Asian Earth Sci. 67–68, 93–113.

Xia, Q.X., Zheng, Y.F., Hu, Z.C., 2010. Trace elements in zircon and coexisting minerals from low-T/UHP metagranite in the Dabie orogen: implications for action of supercritical fluid during continental subduction-zone metamorphism. Lithos 114, 385–413.

Xia, Q.X., Zheng, Y.F., Yuan, H., Wu, F.Y., 2009b. Contrasting Lu–Hf and U–Th–Pb isotope systematics between metamorphic growth and recrystallization of zircon from eclogite-facies metagranites in the Dabie orogen, China. Lithos 112, 477–496.

You, C. F., Castillo, P.R., Gieskes, J.M., Chan, L.H., Spivack, A.J., 1996. Trace element behavior in hydrothermal experiments: implications for fluid processes at shallow depths in subduction zones. Earth Planet. Sci. Lett. 140, 41–52.

Zakharov, D.O., Bindeman, I.N., Serebryakov, N.S., Prave, A.R., Babarina, I.I., 2019. Low-$\delta^{18}O$ rocks in the Belomorian belt, NW Russia, and Scourie dikes, NW Scotland: a record of ancient meteoric water captured by the early Paleoproterozoic global mafic magmatism. Precambrian Res. 333, 105431.

Zhang, S.B., Zheng, Y.F., 2011. On the origin of low $\delta^{18}O$ magmatic rocks. Acta Petrol. Sin. 27, 520–530 (in Chinese with English abstract).

Zhang W., Hu Z.C., 2020. Estimation of isotopic reference values for pure materials and geological reference materials. At. Spectrosc. 4, 93–102.

Zhao, J.H., Li, Q.W., Liu, H., Wang, W., 2018. Neoproterozoic magmatism in the western and northern margins of the Yangtze Block (South China) controlled by slab subduction and subduction-transform-edge-propagator. Earth-Sci. Rev. 187, 1–18.

Zhao, Z.F., Zheng, Y.F., 2003. Calculation of oxygen isotope fractionation in magmaticrocks. Chem. Geol. 193, 59–80.

Zheng, Y.F., Chen, F.K., Gong, B., Zhao, Z.F., 2003. Protolith nature of ultrahigh pressure metamorphic rocks in the Dabie-Sulu orogenic belt: evidence from zircon oxygen isotope and U–Pb age. Chinese Sci. Bull. 48, 110–119.

Zheng, Y.F., Gong, B., Zhao, Z.F., Wu, Y.B., Chen, F.K., 2008. Zircon U–Pb age and O isotope evidence for Neoproterozoic low-^{18}O magmatism during supercontinental rifting in South China: Implications for the snowball earth event. Am. J. Sci. 308, 484–516.

Zheng, Y.F., Wu, Y.B., Chen, F.K., Gong, B., Li, L., Zhao, Z.F., 2004. Zircon U–Pb and oxygen isotope evidence for a large-scale ^{18}O depletion event in igneous rocks during the Neoproterozoic. Geochim. Cosmochim. Acta 68, 4145–4165.

Zheng, Y.F., Wu, Y.B., Gong, B., Chen, R.X., Tang, J., Zhao, Z.F., 2007a. Tectonic driving of Neoproterozoic glaciations: Evidence from extreme oxygen isotope signature of meteoric water in granite. Earth Planet. Sci. Lett. 256, 196–210.

Zheng, Y.F., Zhang, S.B., Zhao, Z.F., Wu, Y.B., Li, X., Li, Z., Wu, F.Y., 2007b. Contrasting zircon Hf and O isotopes in the two episodes of Neoproterozoic granitoids in South China: Implications for growth and reworking of continental crust. Lithos 96, 127–150.

Zheng, Y.F., Zhao, Z.F., Wu, Y.B., Zhang, S.B., Liu, X.M., Wu, F.Y., 2006. Zircon U–Pb age, Hf and O isotope constraints on protolith origin of ultrahigh-pressure eclogite and gneiss in the Dabie orogen. Chem. Geol. 231, 135–158.

Zhou, J.L., Li, X.H., Tang, G.Q., Liu, Y., Tucker, R.D., 2018. New evidence for a continental rift tectonic setting of the Neoproterozoic Imorona-Itsindro Suite (central Madagascar). Precambrian Res. 306, 94–111.

Zhou, J.L., Li, X.H., Tucker, R.D., 2020. New insights into the genesis of Neoproterozoic low-δ^{18}O granitoids in the Seychelles: crustal cannibalization within an intra-plate extensional setting. Sci. Bull. 65, 1880–1883.

Zhu, D.C., Pan, G.T., Mo, X.X., Wang, L.Q., Zhao, Z.D., Liao, Z.L., Geng, Q.R., Dong, G.C., 2006. Identification for the Mesozoic OIB-type basalts in central

Qinghai-Tibetan plateau geochronology, geochemistry and their tectonic setting. Acta Geol. Sinica 9, 1312–1328 (in Chinese with English abstract).

Figure captions

Fig. 1. (a) Major tectonic units of Western Australia (modified after Cawood and Korsch, 2008). Abbreviations: AFO, Albany–Fraser Orogen; CO, Capricorn Orogen; PC, Pilbara Craton; PO, Pinjarra Orogen; YC, Yilgarn Craton. (b) Geological sketch map of the Pinjarra Orogen and surrounding areas, Western Australia (modified after Janssen et al, 2003). Abbreviations: BG, Badgeradda Group; CG, Cardup Group; MBG, Mount Barren Group; MG, Moora Group; NF, Nilling Formation; SRF, Stirling Range Formation.

Fig. 2. Geological sketch map of the Leeuwin Complex, part of the Pinjarra Orogen (modified after Wilde and Murphy, 1990). Sampling localities of the studied metamafic rocks are indicated.

Fig. 3. Field photographs and representative photomicrographs of metamafic rocks from the Leeuwin Complex. (a) Mafic granulite layer (sample D09-2) within syenogranitic gneiss at Rocky Point in the northern Leeuwin Complex. (b) Garnet-bearing amphibolite layer (sample D34-5) within granitic gneiss at Willyabrup Cliffs in the central Leeuwin Complex. (c) Boudinaged mafic granulite layers within granitic gneiss at Cape Naturaliste in the northern Leeuwin Complex. (d–f)

Plane-polarized light photomicrograph of a representative mafic granulite (sample D31-1), garnet-bearing amphibolite (sample D34-5), and amphibolite (sample A14-4) showing typical mineral assemblages. Mineral abbreviations: Bt, biotite; Cpx, clinopyroxene; Grt, garnet; Hbl, hornblende; Op, opaque mineral; Opx, orthopyroxene; Pl, plagioclase; Qtz, quartz.

Fig. 4. Representative cathodoluminescence (CL) images of zircon grains from metamafic rocks from the Leeuwin Complex. (a–d) Zircon from sample D26-2 showing an oscillatory-zoned core and a bright luminescent rim. (e–h) Zircon from sample D31-1 showing an oscillatory-zoned or banded dark core and grey overgrowth rim. (i–l) Zircon from sample D34-1 showing a banded or homogeneous core and a grey luminescent rim. Red solid and yellow dashed circles represent the analytical domains of U–Pb and O isotopes, respectively, and the solid green circles represent Lu–Hf analytical domains. Analyzed spots, apparent $^{206}Pb/^{238}U$ ages, $\delta^{18}O$, and $\varepsilon_{Hf}(t)$ values are provided for each zircon grain. Ages are given at 1σ. Scale bars are 50 μm.

Fig. 5. SHRIMP U–Pb zircon Concordia diagrams for metamafic rocks from the Leeuwin Complex.

Fig. 6. Plots of $\varepsilon_{Hf}(t)$ vs protolith age for zircon grains from metamafic rocks from the Leeuwin Complex.

Fig. 7. (a) Histograms of $\delta^{18}O$ values for magmatic zircon cores with concordant ages from sample D26-2. (b) Histograms of $\delta^{18}O$ values for magmatic zircon cores with concordant ages from sample D31-1. (c) Histograms of $\delta^{18}O$ values for magmatic zircon cores with concordant ages from sample D34-1. (d) Zircon Hf–O isotopes diagram for samples D26-2, D31-1, and D34-1. Shaded fields show the $\delta^{18}O$ range of the mantle zircon (Valley et al., 1998) for comparison.

Fig. 8. (a) Nb/Y vs SiO_2 classification diagram (Winchester and Floyd, 1977). (b) Alkali (Na_2O + K_2O)–FeO^T–MgO (AFM) ternary diagram (Irvine and Baragar, 1971).

Fig. 9. (a) Chondrite-normalized REE patterns for metamafic rocks from the Leeuwin Complex. (b) Primitive mantle-normalized trace element variation diagrams for metamafic rocks from the Leeuwin Complex. Chondrite and primitive mantle-normalized values are from Sun and McDonough (1989). OIB, ocean island basalt; N-MORB, normal mid-ocean ridge basalt; E-MORB, enriched mid-ocean ridge basalt.

Fig. 10. Bivariate plots of selected REEs, HFSEs, and LILEs vs Zr to evaluate the mobility of these elements during later alteration and metamorphism.

Fig. 11. Binary discrimination diagrams. (a) $(Th/Ta)_{PM}$–$(La/Nb)_{PM}$ diagram (Neal et al., 2002; Zhu et al., 2006). Primitive mantle-normalized values (PM) are from Sun

and McDonough (1989). Hawaiian tholeiite and alkali basalts are from http://georocmpch-mainz.gwadg.de/georocl. (b) Th/La vs Nb/Th diagram. (c) Th/La vs Nb/La diagram. (d) La/Sm vs $\varepsilon_{Nd}(t)$ diagram. LCC, lower continental crust; MCC, middle continental crust; UCC, upper continental crust; TCC, total continental crust (Rudnick and Gao, 2003); CLM, continental lithospheric mantle (McDonough, 1990); CAB, continental arc basalt (Kelemen et al., 2007).

Fig. 12. Harker variation diagrams for metamafic rocks from the Leeuwin Complex.

Fig. 13. Mantle source discrimination diagrams for the protoliths of metamafic rocks from the Leeuwin Complex. (a) Ti–Sm–V ternary diagram (Vermeesch, 2006). (b) $(Ta/La)_{PM}$ vs $(Hf/Sm)_{PM}$ diagram (La Flèche et al., 1998), where PM are values normalized to primitive mantle-normalized values. DM, N-MORB, and OIB are from Sun and Mcdonough (1989). (c) La/Yb vs Nb/La diagram (Waston, 1993). E-MORB, N-MORB and OIB are from Sun and Mcdonough (1989). (d) Sm vs Sm/Yb diagram (Aldanmaz et al., 2000). Numbers along curves represent the degree of partial melting. Abbreviations: DM, depleted mantle; E-MORB, enriched mid-ocean ridge basalt; IAB, island arc basalt; MORB, mid-ocean ridge basalt; N-MORB, normal mid-ocean ridge basalt; OIB, ocean island basalt; PM, primitive mantle.

Fig. 14. Tectonic discrimination diagrams for the protoliths of metamafic rocks from the Leeuwin Complex. (a) Zr vs Zr/Y diagram (Pearce and Norry, 1979). WPB, within

plate basalts; MORB, mid-ocean ridge basalts; VAB, volcanic arc basalts. (b) Ta/Hf vs Th/Hf diagram (Wang et al., 2001). I, divergent plate margin, N-MORB; II, convergent plate margin basalts (II_1, ocean island arc basalts; II_2, continental margin volcanic arc basalts); III, oceanic within-plate basalts; IV, continental within-plate basalts (IV_1, intracontinental rift and continental margin rift tholeiites; IV_2, intracontinental rift alkali basalts; IV_3, continental extensional zone or initial rift-related basalts); V, mantle plume basalts. (c) Zr–La–Nb ternary diagram (Cabanis and Lecolle, 1989). 1A, calc-alkali basalts; 1C, volcanic arc basalts; 1B, an area of overlap between 1A and 1C; 2A, continental basalts; 2B, back-arc basin basalts; 3A, alkali basalt from intercontinental rift; 3B/C, E-MORB; 3D, N-MORB. (d)Yb–Th/Ta diagram (Gorton and Schandl, 2000). ACM, active continental margins; WPVZ, within-plate volcanic zones; WPB, within-plate basalts; MORB, mid-ocean ridge basalts.

Fig. 15. In-situ zircon Hf–O isotopic data and assimilation–fractional crystallization (AFC) models fitted to the data. Red points on the AFC curves represent 10% increments in the amount of lowest-$\delta^{18}O$ felsic wall rocks ($\varepsilon_{Hf}(t)$ = 5.4 and $\delta^{18}O$ = 0.42‰; our unpublished data) relative to the original mass of magma. The ratio of Hf contents in the parental magma (OIB; Dobosi et al., 2003; Nowell et al., 1998) and lowest-$\delta^{18}O$ felsic wall rocks end members (Hf_{OIB}/Hf_{WR}) is indicated for each. Shaded fields show the $\delta^{18}O$ range of the mantle zircon (Valley et al., 1998) for comparison.

Fig. 16. Reconstruction of the geodynamic setting for generation of the 674–660 Ma low-$\delta^{18}O$ metamafic rocks in the Leeuwin Complex. See text for detailed interpretation.

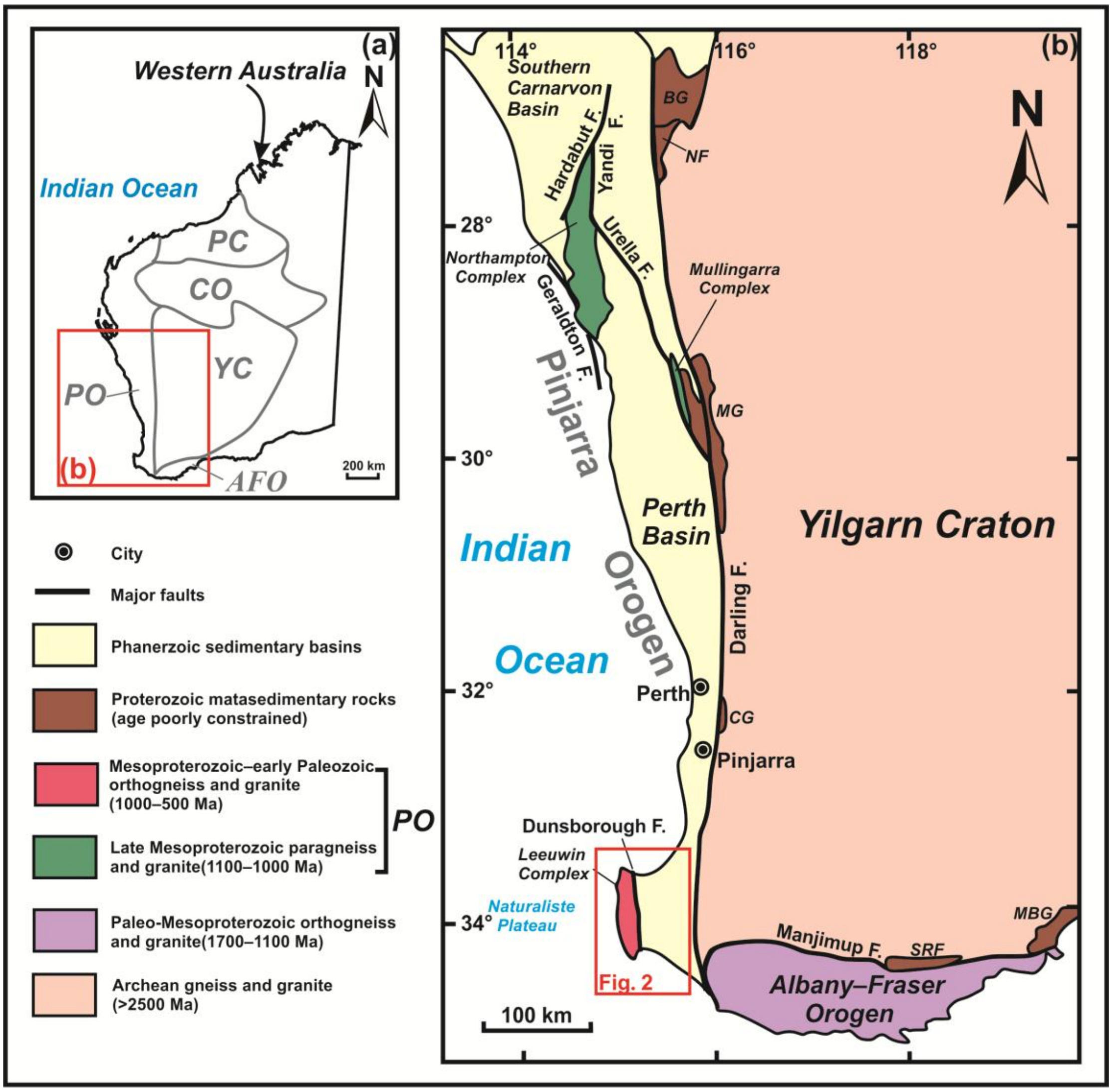
(a)
Western Australia
N
Indian Ocean
PC
CO
YC
PO
AFO
(b)
200 km
City
Major faults
Phanerzoic sedimentary basins
Proterozoic matasedimentary rocks (age poorly constrained)
Mesoproterozoic–early Paleozoic orthogneiss and granite (1000–500 Ma)
Late Mesoproterozoic paragneiss and granite(1100–1000 Ma)
PO
Paleo-Mesoproterozoic orthogneiss and granite(1700–1100 Ma)
Archean gneiss and granite (>2500 Ma)
(b)
114°
116°
118°
Southern Carnarvon Basin
Hardabut F.
Yandi F.
BG
NF
28°
Northampton Complex
Urella F.
Geraldton F.
Mullingarra Complex
MG
Pinjarra
30°
Perth Basin
Yilgarn Craton
Indian
Orogen
Darling F.
Ocean
32°
Perth
CG
Pinjarra
Dunsborough F.
Leeuwin Complex
Naturaliste Plateau
34°
Manjimup F.
SRF
MBG
Fig. 2
Albany–Fraser Orogen
100 km

Figure 1

Figure2 Click here to access/download;Figure;Figure 2.pdf

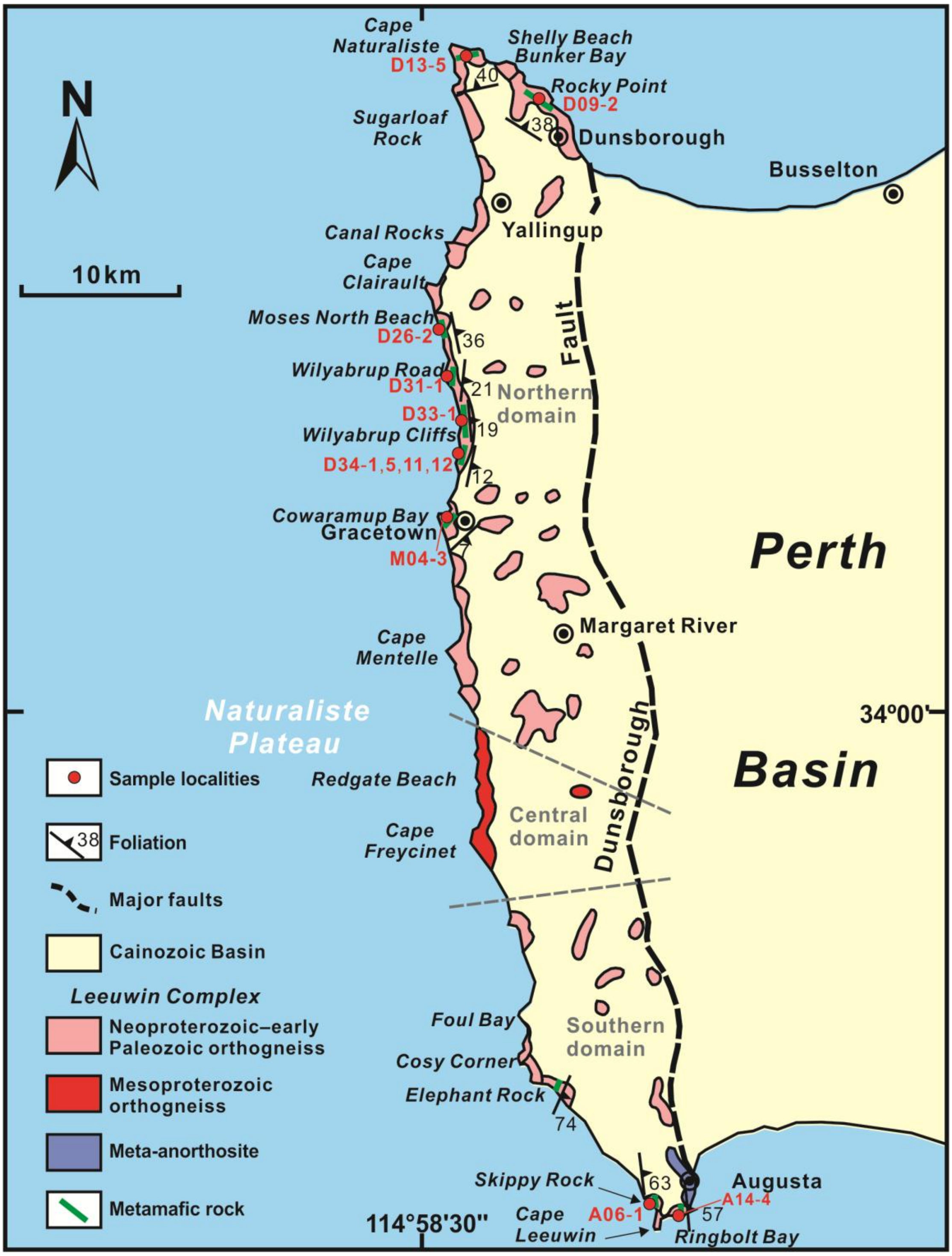

Figure 2

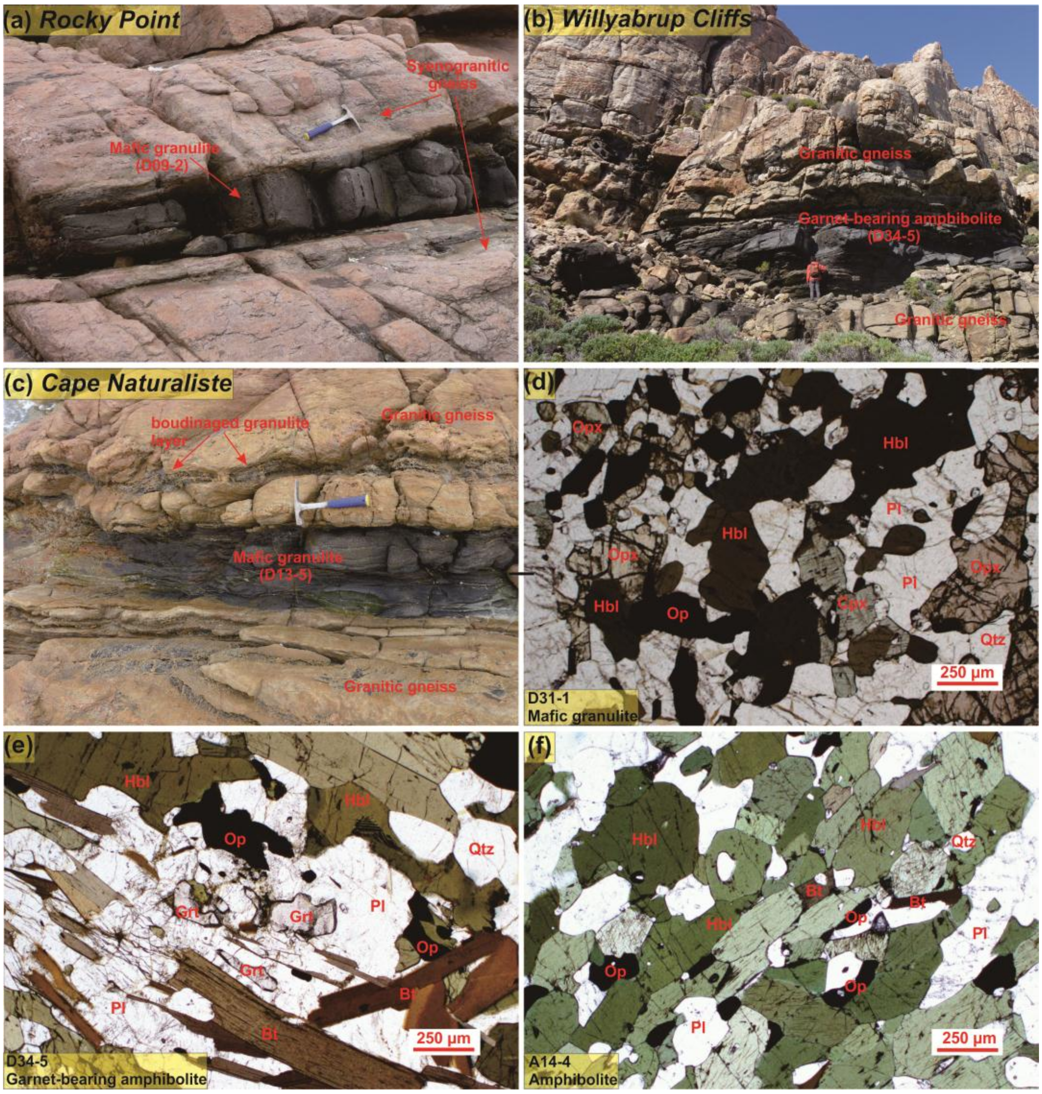
(a) Rocky Point
Syenogranitic gneiss
Mafic granulite (D09-2)
(b) Willyabrup Cliffs
Granitic gneiss
Garnet-bearing amphibolite (D34-5)
Granitic gneiss
(c) Cape Naturaliste
boudinaged granulite layer
Granitic gneiss
Mafic granulite (D13-5)
Granitic gneiss
(d)
Opx
Hbl
Pl
Hbl
Opx
Pl
Opx
Hbl
Op
Cpx
Qtz
250 μm
D31-1
Mafic granulite
(e)
Hbl
Hbl
Op
Qtz
Grt
Grt
Pl
Op
Grt
Bt
Pl
Bt
250 μm
D34-5
Garnet-bearing amphibolite
(f)
Hbl
Hbl
Qtz
Bt
Bt
Op
Hbl
Pl
Op
Op
Pl
250 μm
A14-4
Amphibolite

Figure 3

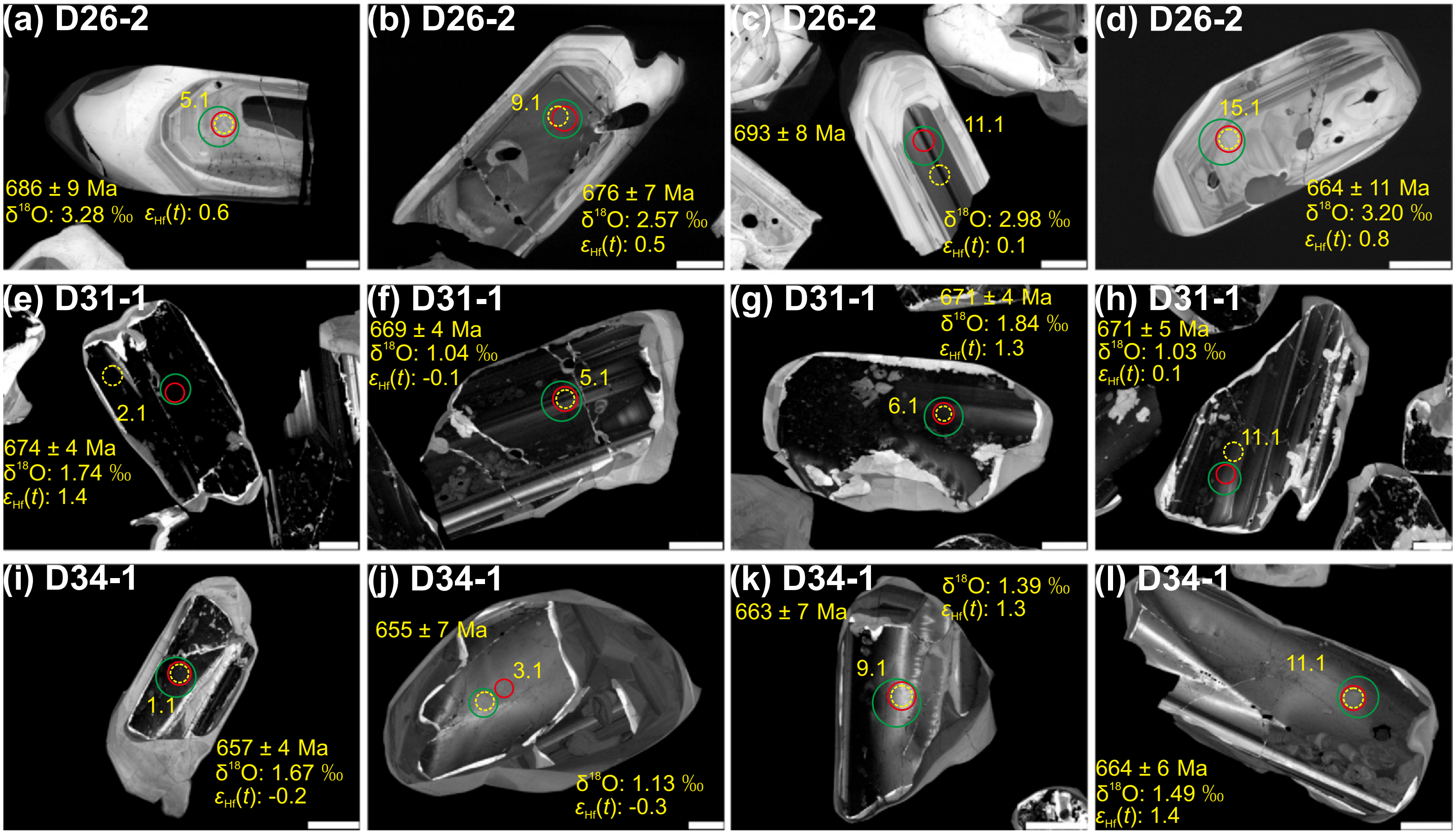

(a) D26-2
5.1
686 ± 9 Ma
δ18O: 3.28 ‰ εHf(t): 0.6
(b) D26-2
9.1
676 ± 7 Ma
δ18O: 2.57 ‰
εHf(t): 0.5
(c) D26-2
693 ± 8 Ma
11.1
δ18O: 2.98 ‰
εHf(t): 0.1
(d) D26-2
15.1
664 ± 11 Ma
δ18O: 3.20 ‰
εHf(t): 0.8
(e) D31-1
2.1
674 ± 4 Ma
δ18O: 1.74 ‰
εHf(t): 1.4
(f) D31-1
669 ± 4 Ma
δ18O: 1.04 ‰
εHf(t): -0.1
5.1
(g) D31-1
671 ± 4 Ma
δ18O: 1.84 ‰
εHf(t): 1.3
6.1
(h) D31-1
671 ± 5 Ma
δ18O: 1.03 ‰
εHf(t): 0.1
11.1
(i) D34-1
1.1
657 ± 4 Ma
δ18O: 1.67 ‰
εHf(t): -0.2
(j) D34-1
655 ± 7 Ma
3.1
δ18O: 1.13 ‰
εHf(t): -0.3
(k) D34-1
δ18O: 1.39 ‰
εHf(t): 1.3
663 ± 7 Ma
9.1
(l) D34-1
11.1
664 ± 6 Ma
δ18O: 1.49 ‰
εHf(t): 1.4

Figure 4

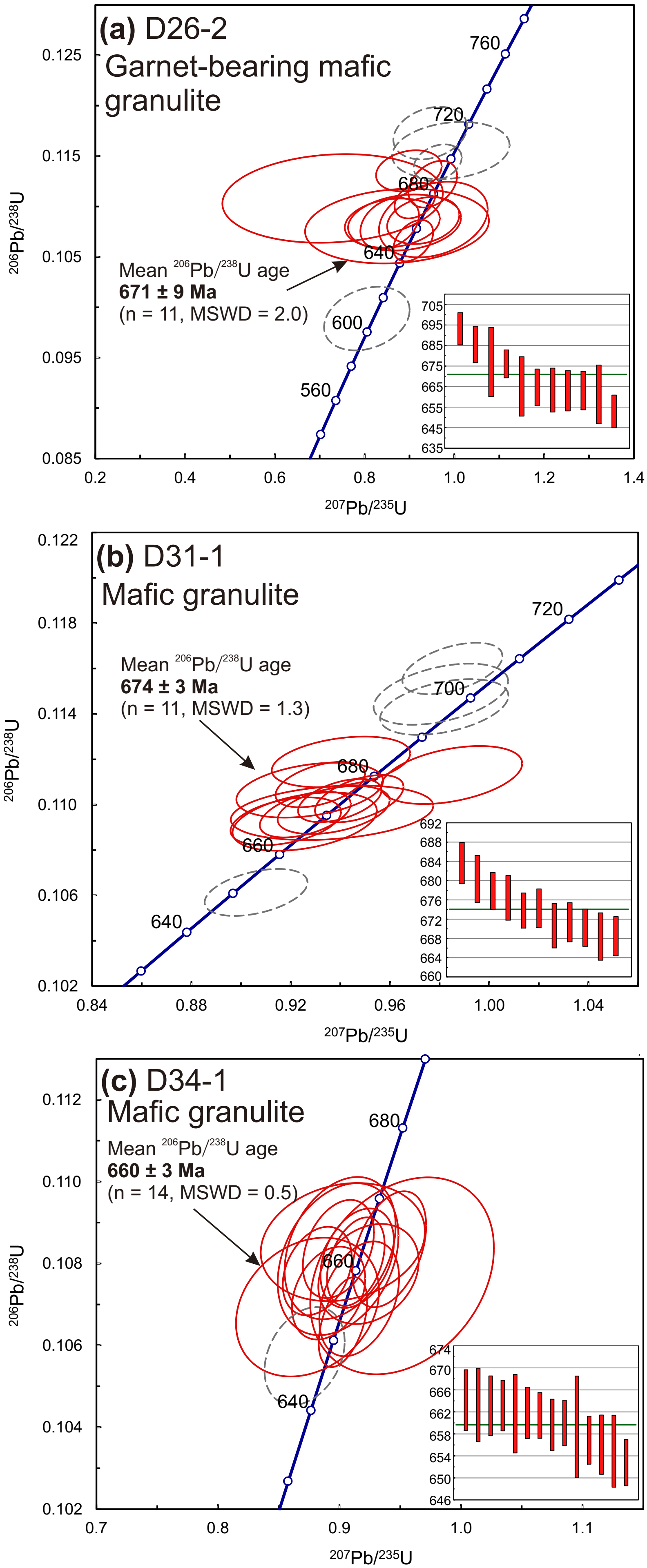
(a) D26-2
Garnet-bearing mafic granulite
Mean 206Pb/238U age
671 ± 9 Ma
(n = 11, MSWD = 2.0)
760
720
680
640
600
560
705
695
685
675
665
655
645
635
0.125
0.115
0.105
0.095
0.085
0.2
0.4
0.6
0.8
1.0
1.2
1.4
206Pb/238U
207Pb/235U
(b) D31-1
Mafic granulite
Mean 206Pb/238U age
674 ± 3 Ma
(n = 11, MSWD = 1.3)
720
700
680
660
640
692
688
684
680
676
672
668
664
660
0.122
0.118
0.114
0.110
0.106
0.102
0.84
0.88
0.92
0.96
1.00
1.04
206Pb/238U
207Pb/235U
(c) D34-1
Mafic granulite
Mean 206Pb/238U age
660 ± 3 Ma
(n = 14, MSWD = 0.5)
680
660
640
674
670
666
662
658
654
650
646
0.112
0.110
0.108
0.106
0.104
0.102
0.7
0.8
0.9
1.0
1.1
206Pb/238U
207Pb/235U

Figure 5

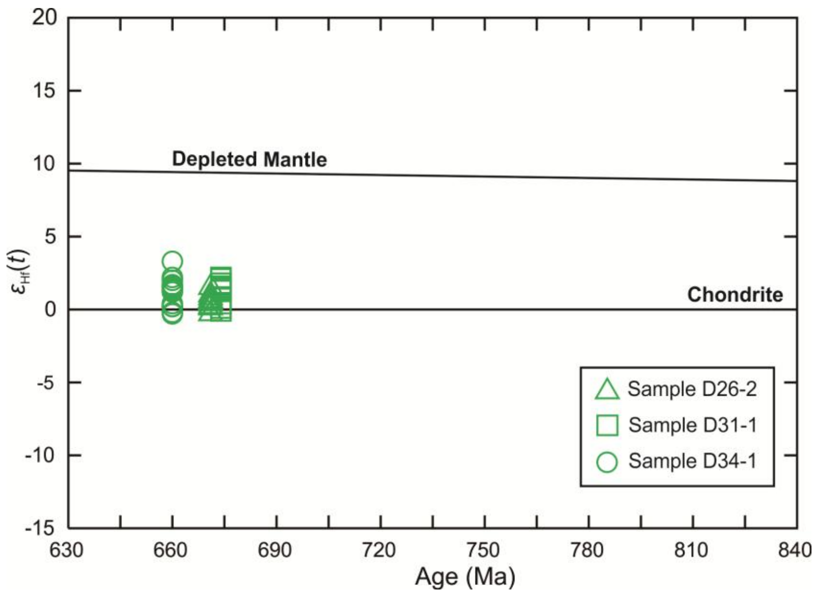
20
15
10
5
0
-5
-10
-15
$\varepsilon_{Hf}(t)$
Depleted Mantle
Chondrite
Sample D26-2
Sample D31-1
Sample D34-1
630
660
690
720
750
780
810
840
Age (Ma)

Figure 6

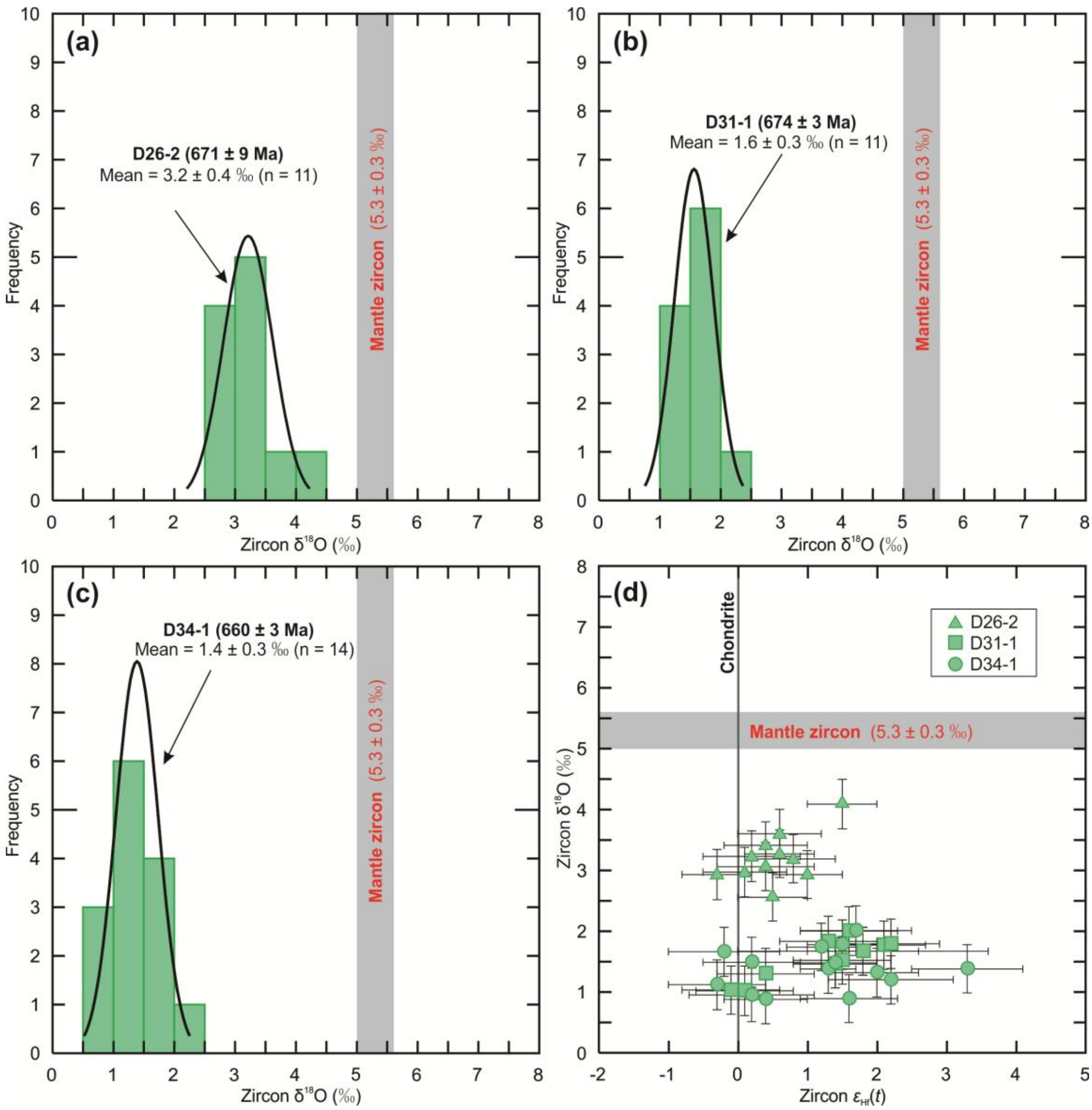

(a)
D26-2 (671 ± 9 Ma)
Mean = 3.2 ± 0.4 ‰ (n = 11)
Mantle zircon (5.3 ± 0.3 ‰)
Frequency
Zircon δ18O (‰)
(b)
D31-1 (674 ± 3 Ma)
Mean = 1.6 ± 0.3 ‰ (n = 11)
(c)
D34-1 (660 ± 3 Ma)
Mean = 1.4 ± 0.3 ‰ (n = 14)
(d)
Chondrite
D26-2
D31-1
D34-1
Zircon εHf(t)

Figure 7

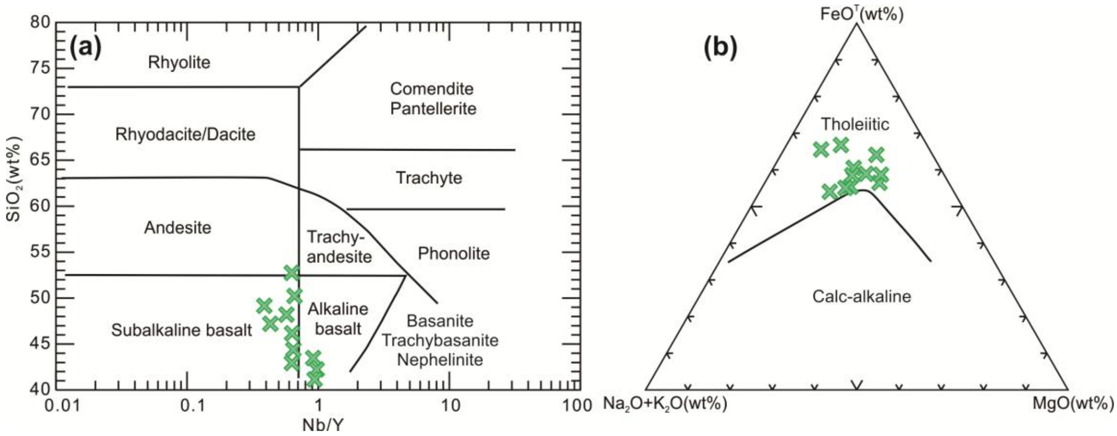
(a)
Rhyolite
Rhyodacite/Dacite
Andesite
Subalkaline basalt
Comendite Pantellerite
Trachyte
Trachy-andesite
Phonolite
Alkaline basalt
Basanite Trachybasanite Nephelinite
SiO_2(wt%)
Nb/Y
80
75
70
65
60
55
50
45
40
0.01
0.1
1
10
100
(b)
FeO^T(wt%)
Tholeiitic
Calc-alkaline
Na_2O+K_2O(wt%)
MgO(wt%)

Figure 8

Figure9

Click here to access/download;Figure;Figure 9.pdf

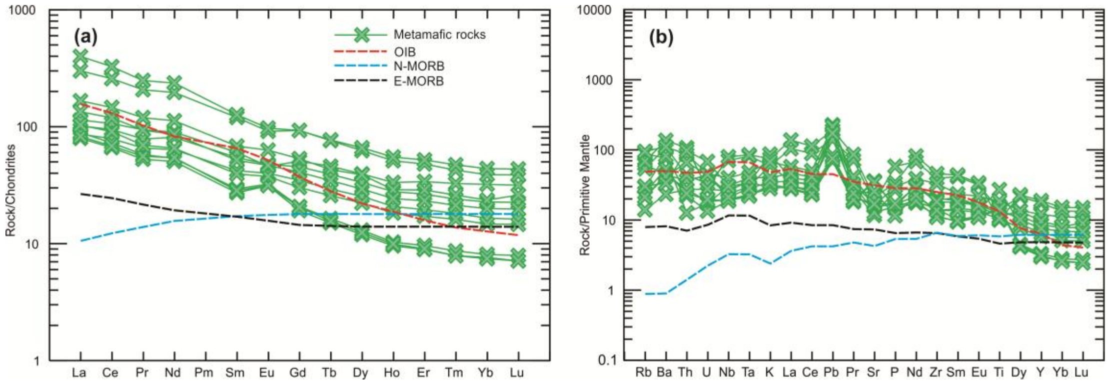

Figure 9

Figure10

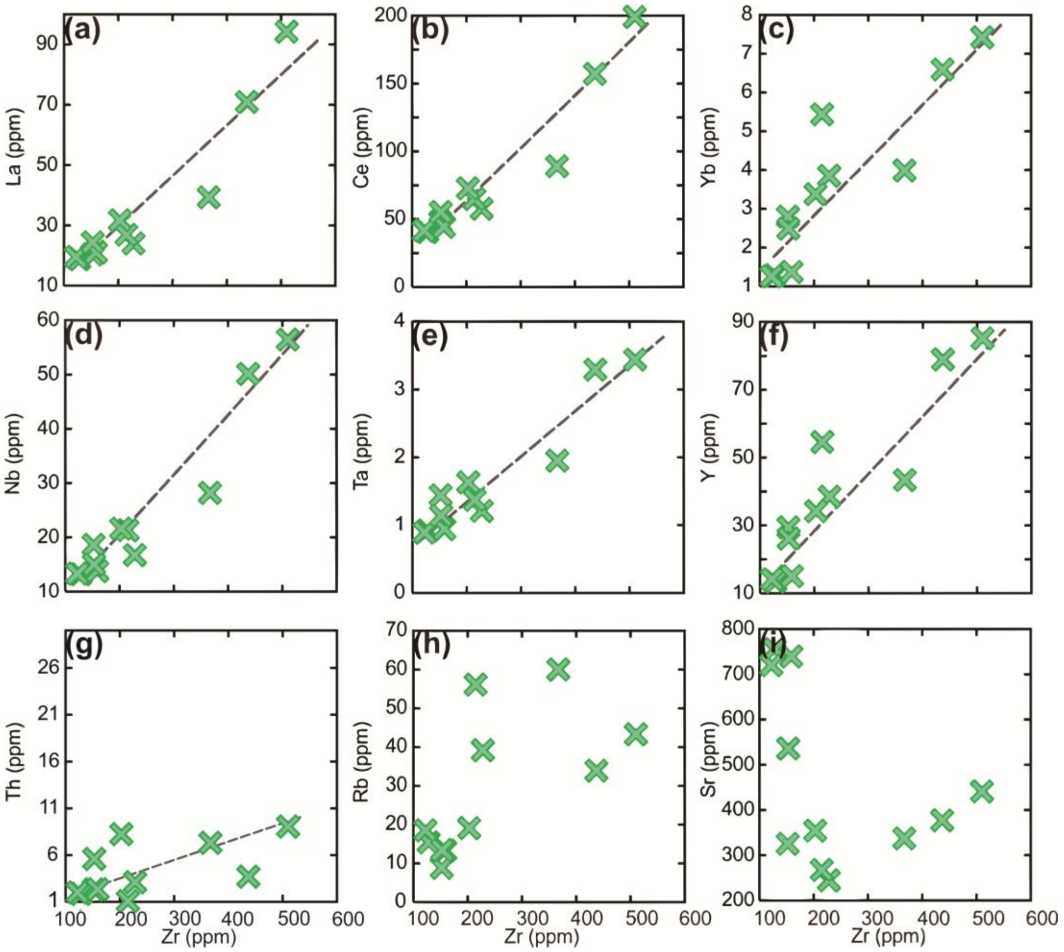

Figure 10

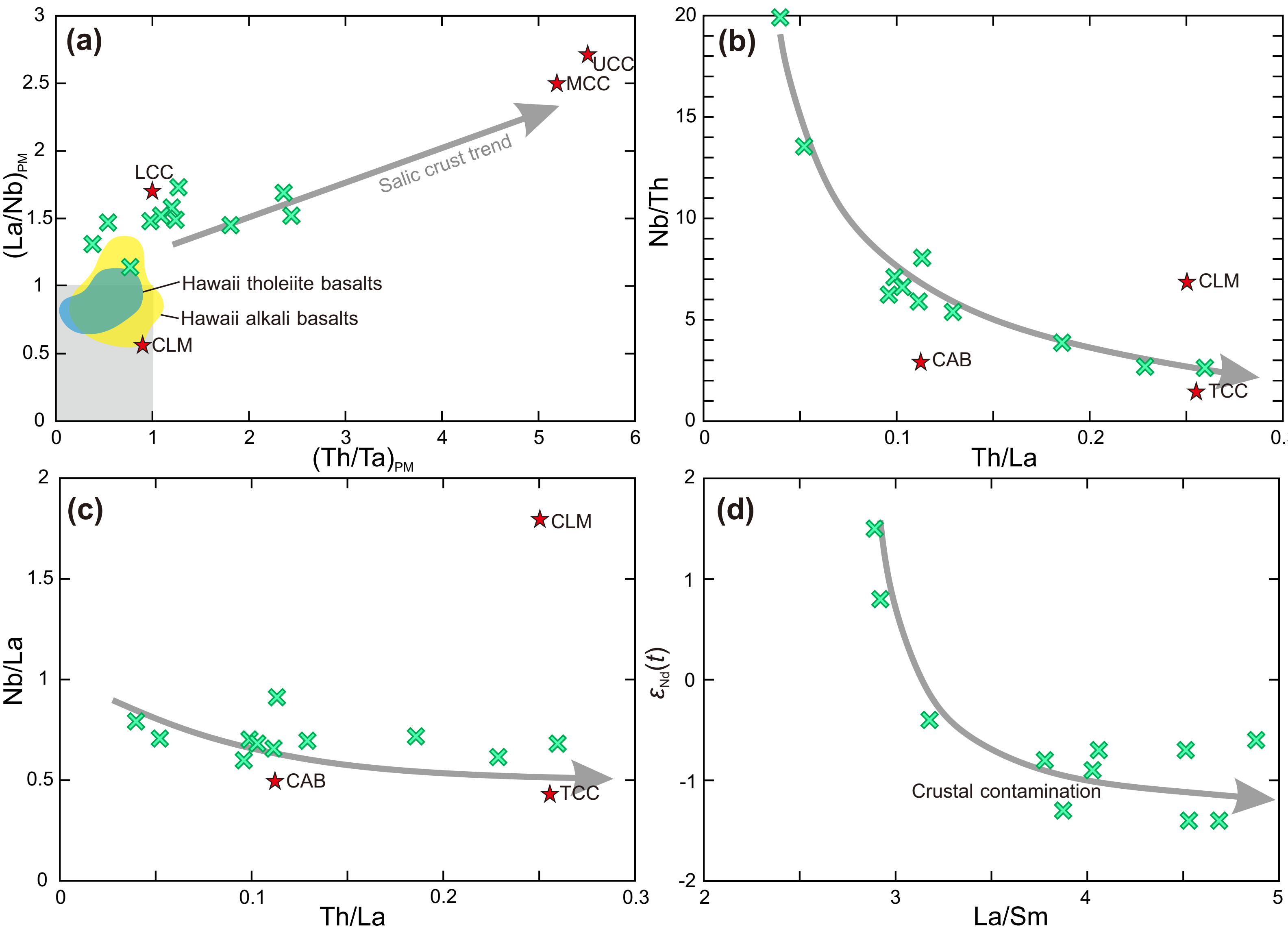
(a)
(La/Nb)$_{PM}$
(Th/Ta)$_{PM}$
UCC
MCC
LCC
CLM
Salic crust trend
Hawaii tholeiite basalts
Hawaii alkali basalts
(b)
Nb/Th
Th/La
CLM
CAB
TCC
(c)
Nb/La
Th/La
CLM
CAB
TCC
(d)
$\varepsilon_{Nd}(t)$
La/Sm
Crustal contamination

Figure 11

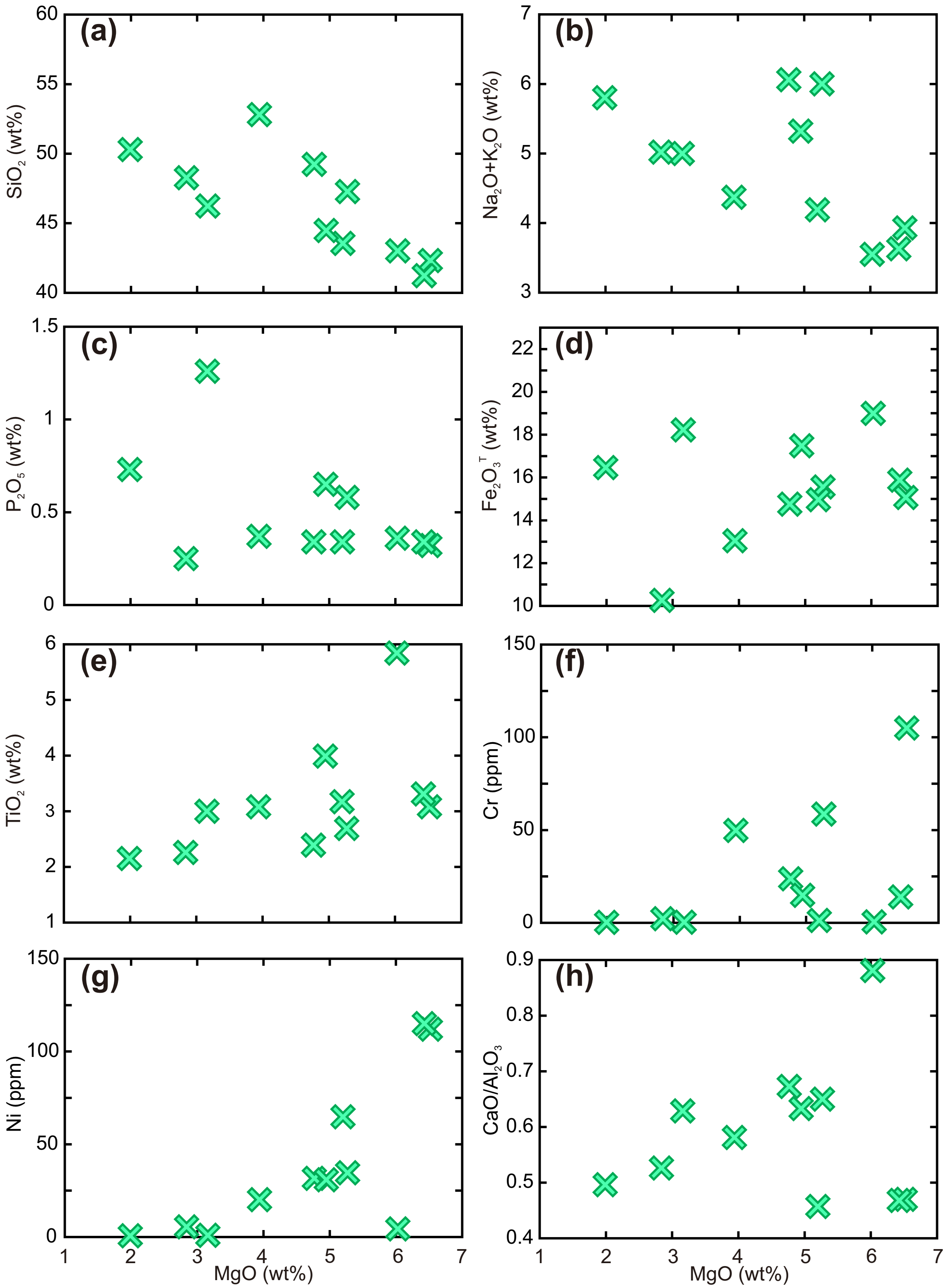
(a)
(b)
(c)
(d)
(e)
(f)
(g)
(h)
SiO2 (wt%)
Na2O+K2O (wt%)
P2O5 (wt%)
Fe2O3T (wt%)
TiO2 (wt%)
Cr (ppm)
Ni (ppm)
CaO/Al2O3
MgO (wt%)
MgO (wt%)

Figure13

Click here to access/download;Figure;Figure 13.pdf

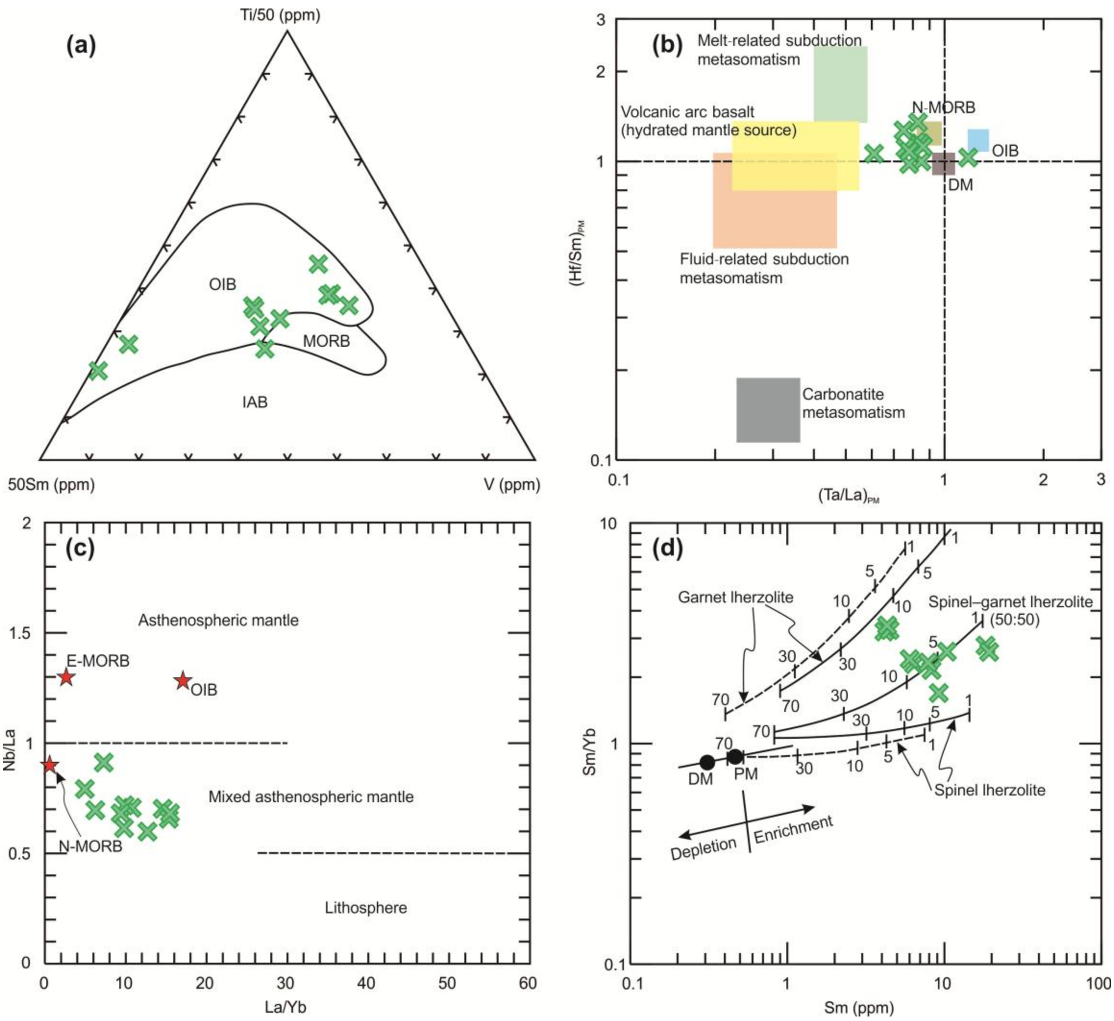

Figure 13

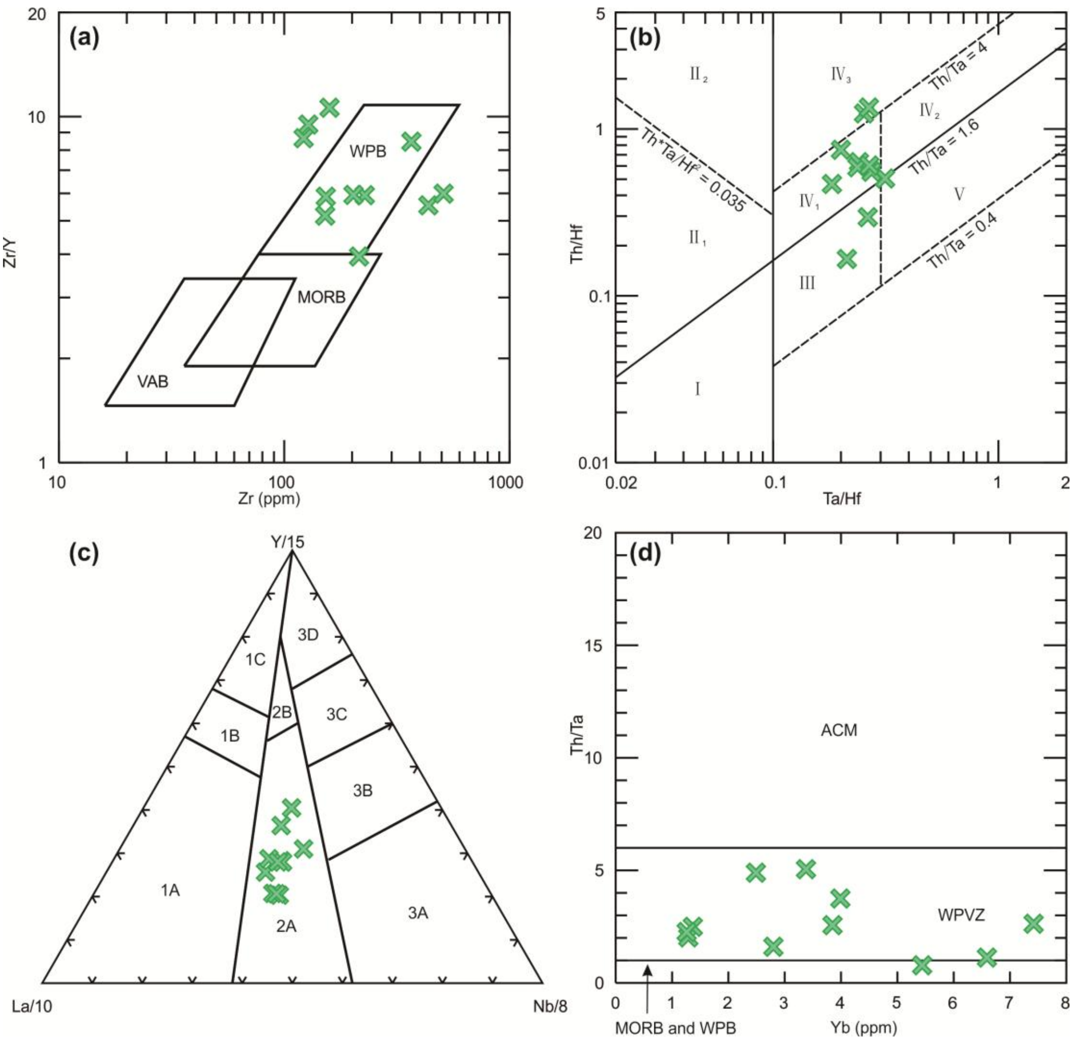
(a)
Zr/Y
Zr (ppm)
WPB
MORB
VAB
(b)
Th/Hf
Ta/Hf
Th*Ta/Hf² = 0.035
Th/Ta = 4
Th/Ta = 1.6
Th/Ta = 0.4
(c)
Y/15
La/10
Nb/8
1A
1B
1C
2A
2B
3A
3B
3C
3D
(d)
Th/Ta
Yb (ppm)
ACM
WPVZ
MORB and WPB

Figure 14

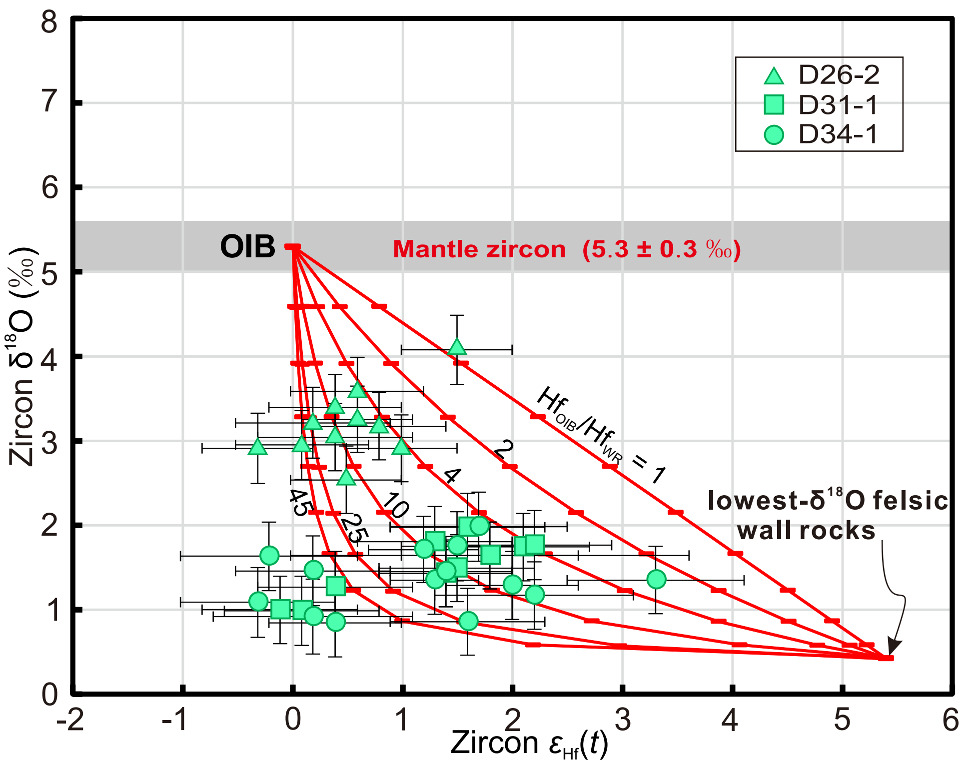

D26-2
D31-1
D34-1
OIB
Mantle zircon (5.3 ± 0.3 ‰)
Hf_{OIB}/Hf_{WR} = 1
2
4
10
25
45
lowest-δ^{18}O felsic wall rocks
Zircon δ^{18}O (‰)
Zircon $\varepsilon_{Hf}(t)$

Figure 15

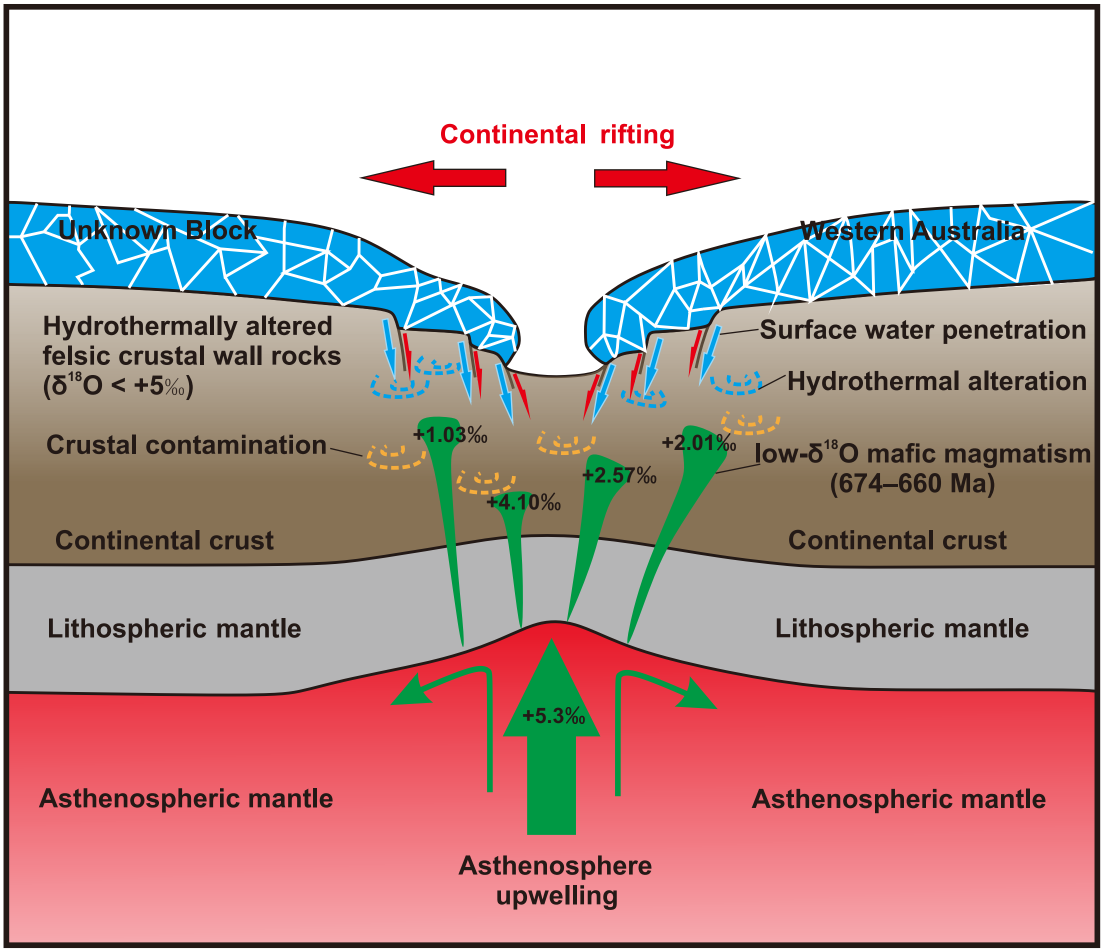

Continental rifting
Unknown Block
Western Australia
Hydrothermally altered felsic crustal wall rocks ($\delta^{18}O$ < +5‰)
Surface water penetration
Hydrothermal alteration
Crustal contamination
+1.03‰
+2.01‰
+2.57‰
+4.10‰
low-$\delta^{18}O$ mafic magmatism (674–660 Ma)
Continental crust
Continental crust
Lithospheric mantle
Lithospheric mantle
+5.3‰
Asthenospheric mantle
Asthenospheric mantle
Asthenosphere upwelling

Figure 16

Table 1

Localities, lithology, mineral assemblages and analytical methods of metamafic rocks from the Leeuwin Complex.

Sample	Location	Coordinates	Mineral modes (vol.%)										SHRIMP dating	Zircon Hf-O	Whole-rock geochemistry	
			Grt	Cpx	Opx	Hbl	Bt	Pl	Kfs	Qtz	Ttn	Op	Potolith ages (Ma)		elements	Nd isotope
D09-2	Rocky Point	S 33°32'46" E 115°03'29"		17		30	2	30	15			6			+	+
D13-5	Cape Naturaliste	S 33°31'54" E 115°00'16"		20		25		50				5			+	+
D26-2	Moses North Beacl	S 33°45'03" E 114°59'33"	5	5		35	1	25	15	2		3	671 ± 9	+		
D31-1	Wilyabrup Road	S 33°47'37" E 115°00'01"		10	18	20		45				7	674 ± 3	+	+	+
D33-1	Wilyabrup Cliffs	S 33°48'07" E 114°59'58"		27		30		35				8			+	+
D34-1	Wilyabrup Cliffs	S 33°48'11" E 114°59'57"		10	10	10	1	60		2		7	660 ± 3	+	+	+
D34-5	Wilyabrup Cliffs	S 33°48'11" E 114°59'57"	7	2		45	7	35				4			+	+
D34-11	Wilyabrup Cliffs	S 33°48'11" E 114°59'57"	25	25			10	33				7			+	+
D34-12	Wilyabrup Cliffs	S 33°48'11" E 114°59'57"	25			30	10	30				5			+	+
M04-3	Cowaramup Bay	S 33°51'28" E 114°59'06"		4		4	1	45				5			+	+
A06-1	Skippy Rock	S 34°21'23" E 115°07'43"				34	1	60			3	2			+	+
A14-4	Ringbolt Bay	S 34°22'04" E 115°09'08"				40	10	40		5		5			+	+

Notes:

Bt, biotite; Cpx, clinopyroxene; Grt, garnet; Hbl, hornblende; Kfs, K-feldspar; Op,opaque mineral; Opx, orthopyroxene; Pl, plagioclase; Qtz, quartz.

Cross symbols show samples for zircon Hf-O and whole-rock geochemical analyses.

Table 2

SHRIMP U–Pb zircon analyses for metamafic rocks from the Leeuwin Complex.

Spot	U (ppm	Th (ppm)	Th/U	Pb* (ppm)	Common ^{206}Pb (%)	Isotopic ratios ^{207}Pb/^{206}Pb	±σ(%)	^{207}Pb/^{235}U	±σ(%)	^{206}Pb/^{238}U	±σ(%)	Ages (Ma) ^{206}Pb/^{238}U	±σ	^{207}Pb/^{206}Pb	±σ	Discordance(%)
Sample D26-2 (garnet-bearing mafic granulite)																
1.1	47	48	1.06	4.7	0.00	0.0623	8.6	0.992	8.7	0.1156	1.6	705	11	684	183	-3
2.1	22	30	1.44	2.0	0.64	0.0636	8.1	0.953	8.4	0.1087	2.3	665	14	728	171	9
3.1	20	15	0.77	1.9	2.30	0.0477	22.2	0.728	22.3	0.1107	2.6	677	17	84	526	-88
4.1	25	30	1.21	2.4	1.33	0.0585	15.4	0.872	15.5	0.1080	2.3	661	14	550	336	-17
5.1	59	60	1.05	5.7	0.43	0.0615	3.5	0.952	3.8	0.1122	1.4	686	9	657	75	-4
6.1	51	68	1.37	5.2	0.68	0.0585	5.6	0.946	5.7	0.1173	1.5	715	10	549	121	-23
7.1	26	21	0.84	2.2	0.79	0.0590	7.5	0.805	7.8	0.0989	2.1	608	12	569	164	-6
8.1	59	84	1.47	5.6	0.53	0.0621	5.5	0.930	5.7	0.1086	1.4	665	9	679	118	2
9.1	118	169	1.48	11.3	0.40	0.0598	3.1	0.912	3.3	0.1106	1.1	676	7	597	67	-12
10	112	146	1.34	11.0	0.00	0.0611	3.5	0.963	3.7	0.1143	1.0	698	7	642	76	-8
11	91	123	1.39	9.0	0.73	0.0574	5.2	0.898	5.4	0.1135	1.2	693	8	507	115	-27
12	48	63	1.36	4.5	0.47	0.0573	4.8	0.856	5.0	0.1083	1.5	663	10	503	106	-24
13	57	76	1.38	5.4	0.72	0.0577	8.0	0.861	8.1	0.1083	1.5	663	9	517	175	-22
14	100	103	1.06	9.2	0.13	0.0618	2.9	0.908	3.2	0.1066	1.3	653	8	667	63	2
15	41	43	1.08	3.8	0.97	0.0595	9.2	0.889	9.4	0.1084	1.7	663	11	584	200	-12
Sample D31-1 (mafic granulite)																
1.1	342	528	1.60	32.6	0.29	0.0608	2.0	0.928	2.1	0.1106	0.7	676	5	633	43	-6
2.1	615	1010	1.70	58.3	0.10	0.0623	1.1	0.948	1.2	0.1103	0.6	674	4	685	23	2
3.1	482	790	1.69	44.0	0.22	0.0619	1.4	0.906	1.5	0.1061	0.6	650	4	671	29	3
4.1	251	319	1.31	23.7	0.26	0.0614	1.9	0.926	2.1	0.1092	0.8	668	5	655	41	-2
5.1	517	994	1.99	48.7	0.21	0.0609	1.5	0.918	1.6	0.1093	0.6	668	4	637	32	-5
6.1	495	634	1.32	46.8	0.21	0.0619	1.5	0.937	1.6	0.1098	0.6	671	4	672	31	0
7.1	909	1571	1.78	86.2	0.12	0.0619	1.0	0.940	1.2	0.1102	0.6	674	4	669	22	-1
8.1	272	345	1.31	26.1	0.12	0.0642	1.7	0.985	1.9	0.1113	0.8	680	5	747	37	10
9.1	705	1258	1.84	67.3	0.13	0.0610	1.1	0.932	1.3	0.1109	0.6	678	4	638	24	-6
10	330	476	1.49	32.5	0.14	0.0623	1.6	0.982	1.7	0.1143	0.7	698	5	684	34	-2
11	316	492	1.61	29.8	0.28	0.0620	2.8	0.937	2.9	0.1096	0.7	671	5	673	60	0
12	463	928	2.07	44.6	0.19	0.0609	1.8	0.940	2.0	0.1119	0.7	684	4	637	40	-7
13	394	569	1.49	39.0	0.16	0.0619	1.7	0.980	1.8	0.1149	0.8	701	5	671	35	-4
14	669	1340	2.07	66.8	0.14	0.0616	1.2	0.985	1.4	0.1160	0.6	708	4	660	25	-7
15	720	1215	1.74	67.9	0.14	0.0613	1.2	0.926	1.3	0.1096	0.6	670	4	649	25	-3
Sample D34-1 (mafic granulite)																
1.1	376	392	1.08	34.7	0.36	0.0602	2.1	0.891	2.2	0.1073	0.7	657	4	612	46	-7
2.1	168	183	1.13	15.7	0.25	0.0630	1.9	0.941	2.1	0.1083	0.9	663	5	708	41	7
3.1	108	96	0.92	10.0	0.46	0.0593	4.3	0.874	4.5	0.1069	1.0	655	7	577	94	-12
4.1	440	608	1.43	40.9	0.37	0.0593	2.0	0.882	2.1	0.1078	0.7	660	4	579	44	-12
5.1	273	345	1.31	25.4	0.24	0.0613	2.1	0.915	2.2	0.1081	0.7	662	5	651	44	-2
6.1	364	415	1.18	33.3	0.00	0.0614	1.3	0.903	1.5	0.1066	0.7	653	4	655	28	0
7.1	285	316	1.14	26.0	0.22	0.0598	2.4	0.871	2.5	0.1057	0.7	648	5	595	52	-8
8.1	231	262	1.17	21.6	0.78	0.0641	5.0	0.951	5.3	0.1077	1.5	659	9	744	107	13
9.1	144	131	0.94	13.5	0.38	0.0603	3.2	0.900	3.4	0.1084	1.1	663	7	613	69	-8
10	459	714	1.61	42.7	0.23	0.0613	1.6	0.913	1.7	0.1080	0.7	661	4	650	34	-2
11	174	186	1.11	16.2	0.44	0.0603	4.9	0.903	4.9	0.1085	0.9	664	6	616	105	-7
12	267	312	1.21	24.8	0.09	0.0622	2.9	0.924	3.0	0.1077	0.7	660	5	681	61	3
13	298	382	1.33	27.8	0.29	0.0602	2.0	0.899	2.1	0.1083	0.7	663	5	610	44	-8
14	171	184	1.11	15.8	0.47	0.0620	2.2	0.916	2.4	0.1071	0.9	656	5	675	47	3
15	84	60	0.74	7.9	0.57	0.0603	3.5	0.899	3.7	0.1081	1.1	662	7	614	75	-7

Pb* denotes radiogenic Pb. Common ^{206}Pb (%) represents the proportion of common ^{206}Pb in total ^{206}Pb measured. Common Pb was corrected using the measured ^{204}Pb. All uncertainties are 1σ.

Table 3

SHRIMP zircon O and LA–MC–ICP–MS Lu–Hf isotopic analyses of magmatic zircon cores from metamafic rocks from the Leeuwin Complex.

Spot	Age (Ma)	^{176}Yb/^{177}Hf	±2σ	^{176}Lu/^{177}Hf	±2σ	^{176}Hf/^{177}Hf	±2σ	$f_{Lu/Hf}$	$\varepsilon_{Hf}(0)$	$\varepsilon_{Hf}(t)$	2σ	T_{DM} (Ma)	δ^{18}O (‰)	2σ
Sample D26-2 (garnet-bearing mafic granulite)														
1.1	704	0.01298	0.00029	0.00045	0.000012	0.282393	0.000035	-0.99	-13.4	1.9	1.2	1196	2.98	0.79
2.1	671	0.00632	0.00015	0.0002364	0.0000072	0.282398	0.000027	-0.99	-13.2	1.5	1.0	1183	4.10	0.81
3.1	671	0.00978	0.0002	0.0003397	0.0000089	0.28235	0.000026	-0.99	-14.9	-0.3	0.9	1252	2.94	0.82
4.1	671	0.01978	0.00074	0.00066	0.000027	0.282378	0.000032	-0.98	-13.9	0.6	1.1	1223	3.61	0.80
5.1	671	0.01455	0.00019	0.0004892	0.0000026	0.282376	0.00003	-0.99	-14.0	0.6	1.1	1221	3.28	0.78
6.1	704	0.0345	0.002	0.001165	0.000082	0.282393	0.000039	-0.96	-13.4	1.6	1.4	1219	3.44	0.78
8.1	671	0.023	0.0011	0.00076	0.000037	0.282374	0.000039	-0.98	-14.1	0.4	1.4	1232	3.07	0.79
9.1	671	0.0405	0.0028	0.001275	0.000072	0.282385	0.000028	-0.96	-13.7	0.5	1.0	1234	2.57	0.79
10.1	704	0.01445	0.0007	0.000455	0.000014	0.282332	0.000028	-0.99	-15.6	-0.2	1.0	1280	3.52	0.80
11.1	671	0.0269	0.0042	0.00083	0.0001	0.282368	0.000035	-0.98	-14.3	0.1	1.2	1243	2.98	0.81
12.1	671	0.02	0.002	0.000676	0.000056	0.282367	0.000037	-0.98	-14.3	0.2	1.3	1239	3.24	0.83
13.1	671	0.0164	0.00065	0.000544	0.000024	0.282372	0.000035	-0.98	-14.1	0.4	1.2	1228	3.42	0.78
14.1	671	0.025	0.0021	0.000789	0.000052	0.282392	0.000031	-0.98	-13.4	1.0	1.1	1208	2.94	0.78
15.1	671	0.0205	0.0014	0.000659	0.000045	0.282385	0.000034	-0.98	-13.7	0.8	1.2	1214	3.20	0.79
Sample D31-1 (mafic granulite)														
1.1	674	0.1079	0.0021	0.0026	0.000077	0.282397	0.00004	-0.92	-13.3	0.4	1.4	1261	1.31	0.83
2.1	674	0.1344	0.0055	0.00377	0.00019	0.282439	0.000035	-0.89	-11.8	1.4	1.2	1240	1.47	0.78
4.1	674	0.0785	0.0066	0.00221	0.00016	0.282424	0.000042	-0.93	-12.3	1.6	1.5	1209	2.01	0.80
5.1	674	0.0876	0.0019	0.002507	0.000065	0.28238	0.000037	-0.92	-13.9	-0.1	1.3	1283	1.04	0.79
6.1	674	0.1056	0.004	0.002658	0.000067	0.282422	0.000039	-0.92	-12.4	1.3	1.4	1227	1.84	0.83
7.1	674	0.1567	0.0023	0.003578	0.000098	0.282447	0.000047	-0.89	-11.5	1.8	1.7	1221	1.68	0.79
8.1	674	0.0855	0.0025	0.002507	0.000052	0.282443	0.000035	-0.92	-11.6	2.1	1.2	1191	1.78	0.79
9.1	674	0.1111	0.0057	0.00297	0.00018	0.28244	0.0001	-0.91	-11.7	1.8	3.5	1211	1.68	0.78
10.1	702	0.0859	0.003	0.00214	0.00011	0.282379	0.000033	-0.94	-13.9	0.6	1.2	1271	1.43	0.86
11.1	674	0.1009	0.0052	0.00278	0.00011	0.282389	0.00004	-0.92	-13.5	0.1	1.4	1279	1.03	0.81
12.1	674	0.103	0.012	0.00287	0.0003	0.28243	0.000041	-0.91	-12.1	1.5	1.5	1222	1.53	0.79
13.1	702	0.098	0.016	0.00258	0.0004	0.282414	0.000043	-0.92	-12.7	1.6	1.5	1236	1.78	0.80
14.1	702	0.129	0.013	0.00347	0.00028	0.282459	0.000046	-0.90	-11.1	2.8	1.6	1199	1.48	0.81
15.1	674	0.1113	0.0053	0.00273	0.000081	0.282448	0.000037	-0.92	-11.5	2.2	1.3	1191	1.80	0.81
Sample D34-1 (mafic granulite)														

1.1	660	0.0646	0.0073	0.00198	0.00024	0.28238	0.000047	-0.94	-13.9	-0.2	1.7	1264	1.67	0.80
2.1	660	0.059	0.019	0.0016	0.00048	0.282426	0.000042	-0.95	-12.2	1.6	1.5	1186	0.90	0.79
3.1	660	0.0534	0.0076	0.00155	0.0002	0.28237	0.000041	-0.95	-14.2	-0.3	1.5	1264	1.13	0.82
4.1	660	0.0892	0.0065	0.00234	0.00013	0.282396	0.000049	-0.93	-13.3	0.2	1.7	1254	0.96	0.88
5.1	660	0.0563	0.0026	0.001751	0.000074	0.282429	0.000046	-0.95	-12.1	1.7	1.6	1187	2.02	0.81
6.1	660	0.0907	0.0055	0.00274	0.00015	0.282487	0.000045	-0.92	-10.1	3.3	1.6	1134	1.39	0.79
8.1	660	0.073	0.015	0.00205	0.00039	0.282443	0.000036	-0.94	-11.6	2.0	1.3	1176	1.33	0.80
9.1	660	0.0075	0.00093	0.000242	0.000028	0.2824	0.000024	-0.99	-13.2	1.3	0.8	1180	1.39	0.80
10.1	660	0.088	0.012	0.00248	0.00028	0.282397	0.000040	-0.93	-13.3	0.2	1.4	1257	1.50	0.82
11.1	660	0.0495	0.008	0.00144	0.0002	0.282418	0.000036	-0.96	-12.5	1.4	1.3	1192	1.49	0.83
12.1	660	0.0296	0.0065	0.00084	0.00016	0.282412	0.000030	-0.97	-12.7	1.5	1.1	1182	1.79	0.81
13.1	660	0.0541	0.0051	0.00175	0.00019	0.282417	0.000027	-0.95	-12.6	1.2	1.0	1204	1.75	0.78
14.1	660	0.0263	0.0062	0.00075	0.00014	0.28238	0.000035	-0.98	-13.9	0.4	1.2	1224	0.89	0.80
15.1	660	0.088	0.011	0.00257	0.00029	0.282454	0.000050	-0.92	-11.2	2.2	1.8	1177	1.21	0.79

Table 4

Major and trace element compositions of metamafic rocks from the Leeuwin Complex.

Sample	D09-2	D13-5	D31-1	D33-1	D34-1	D34-5	D34-11	D34-12	M04-3	A06-1	A14-4
Major elements (wt.%)											
SiO_2	47.28	49.23	46.23	43.01	50.29	42.31	43.55	41.23	44.47	48.27	52.81
TiO_2	2.69	2.39	3	5.84	2.15	3.08	3.17	3.31	3.99	2.26	3.08
Al_2O_3	13.37	12.96	13.87	12.19	14.63	19.11	19.32	19.11	13.73	20.34	14.27
$Fe_2O_3^T$	15.55	14.75	18.22	18.99	16.46	15.06	14.96	15.87	17.48	10.26	13.04
MnO	0.22	0.25	0.29	0.25	0.28	0.15	0.16	0.15	0.25	0.14	0.18
MgO	5.27	4.77	3.16	6.03	1.99	6.52	5.2	6.43	4.95	2.84	3.94
CaO	8.69	8.72	8.72	10.74	7.26	8.98	8.83	8.94	8.69	10.7	8.29
Na_2O	4.2	3.47	3.21	2.71	3.56	3	3.35	2.67	3.3	3.98	3.17
K_2O	1.8	2.59	1.79	0.84	2.24	0.93	0.84	0.96	2.02	1.04	1.2
P_2O_5	0.58	0.34	1.26	0.36	0.73	0.32	0.34	0.34	0.65	0.25	0.37
LOI	0.11	0.06	-0.71	-0.05	-0.48	0.16	0.25	0.18	-0.14	0.23	-0.09
TOTAL	99.76	99.53	99.04	100.91	99.11	99.62	99.97	99.19	99.39	100.31	100.26
Mg#	44.1	43.0	28.8	42.5	22.0	50.2	44.8	48.6	39.8	39.2	41.3
Trace elements (ppm)											
Sc	33.9	36.2	35.3	49.5	30.5	12.6	13.4	14.8	28.9	22.5	28.8
V	300	360	59.8	513	18.2	377	386	490	334	199	360
Cr	58.6	23.7	0.31	0.43	0.19	105	1.24	13.9	14.8	2.17	49.8
Co	42.3	49.5	29.1	54.7	21.5	70	59.8	78.3	49.3	28	38.5
Ni	34.6	31.6	0.86	4.36	0.62	112	64.8	115	30.8	5.44	20.1
Cu	32.5	54.7	6.04	50.8	13.6	14.4	49.8	44.2	3.85	3.63	1.55
Zn	125	155	213	134	292	113	108	122	198	106	114
Ga	20.7	22.4	27.8	20.9	30.6	21.2	21.1	23	22.8	26.4	24.8
Rb	39.2	56.1	33.9	8.83	43.3	15.4	13.3	18.5	60	13.4	19.1
Sr	244	267	377	325	441	755	739	720	337	536	354
Y	38.5	54.6	78.9	29.4	85.2	13.5	15	14.1	43.4	26.1	34.2
Zr	228	215	437	152	510	128	159	122	367	153	203
Nb	16.7	21.3	50.1	18.6	56.4	13.2	13.8	13.3	28.2	15	21.6
Ba	305	525	755	162	947	374	309	575	770	291	233
La	24	26.9	70.9	20.4	94.2	18.8	21	19.5	39.3	24.4	31.7
Ce	57.7	64.9	157	48.2	199	40.4	44.3	41.6	89	55.3	72.6
Pr	7.44	8.91	19.6	6.22	23.5	4.98	5.47	5.28	11.3	6.58	8.85
Nd	37.7	41.8	91.3	29.6	110	23.5	24.9	25.3	52.3	30.5	40
Sm	8.3	9.21	18.3	6.42	19.3	4.15	4.48	4.32	10.4	6.01	7.87
Eu	2.76	2.65	5.28	2.31	5.62	1.81	1.87	1.82	3.64	2.17	2.7
Gd	9.29	10.4	19	7.12	19	3.92	4.25	4.19	10.9	6.18	8.36
Tb	1.46	1.71	2.83	1.09	2.87	0.56	0.61	0.58	1.6	0.96	1.29
Dy	8.44	9.98	15.8	6.43	16.7	3.02	3.3	3.15	9.83	5.63	7.41
Ho	1.57	1.88	2.88	1.17	3.1	0.54	0.58	0.56	1.63	1.03	1.37
Er	4.37	5.6	7.91	3.22	8.57	1.47	1.59	1.49	4.74	2.83	3.83
Tm	0.61	0.83	1.08	0.46	1.2	0.2	0.22	0.2	0.66	0.41	0.54
Yb	3.85	5.44	6.59	2.8	7.42	1.29	1.37	1.26	3.99	2.49	3.38
Lu	0.57	0.8	0.98	0.41	1.1	0.18	0.2	0.18	0.66	0.37	0.5
Hf	6.63	6.44	12.5	4.58	14.3	3.36	3.97	3.33	9.74	4.5	6.12
Ta	1.21	1.37	3.29	1.44	3.44	0.92	0.94	0.89	1.95	1.14	1.63
Pb	9.94	16	9.86	5.64	13.4	4.87	5.88	5.29	15.2	12.3	12.1
Th	3.1	1.07	3.7	2.31	9.04	1.86	2.34	2.01	7.3	5.58	8.23

U	0.91	0.36	0.69	0.57	0.58	0.28	0.38	0.41	0.96	0.92	1.42
ΣREE	168.06	191.01	419.45	135.85	511.58	104.82	114.14	109.43	239.95	144.86	190.4
LREE	137.9	154.37	362.38	113.15	451.62	93.64	102.02	97.82	205.94	124.96	163.72
HREE	30.16	36.64	57.07	22.7	59.96	11.18	12.12	11.61	34.01	19.9	26.68
LREE/HREE	4.57	4.21	6.35	4.98	7.53	8.38	8.42	8.43	6.06	6.28	6.14
$(La/Yb)_N$	4.47	3.55	7.72	5.23	9.11	10.45	11.00	11.10	7.07	7.03	6.73
$(La/Sm)_N$	1.87	1.89	2.50	2.05	3.15	2.92	3.03	2.91	2.44	2.62	2.60
$(Gd/Yb)_N$	2.00	1.58	2.39	2.10	2.12	2.51	2.57	2.75	2.26	2.05	2.05
$(Dy/Yb)_N$	1.47	1.23	1.60	1.54	1.51	1.57	1.61	1.67	1.65	1.51	1.47
$(Th/Ta)_{PM}$	1.24	0.38	0.54	0.77	1.27	0.98	1.20	1.09	1.81	2.36	2.44
$(La/Nb)_{PM}$	1.49	1.31	1.47	1.14	1.73	1.48	1.58	1.52	1.45	1.69	1.52
$(Ta/La)_{PM}$	0.84	0.85	0.78	1.18	0.61	0.82	0.75	0.76	0.83	0.78	0.86
$(Hf/Sm)_{PM}$	1.15	1.00	0.98	1.03	1.06	1.16	1.27	1.11	1.35	1.08	1.12
$(Ce/Ce^*)_{PM}$	1.06	1.03	1.03	1.05	1.04	1.02	1.01	1.01	1.04	1.07	1.06
Nb/Nb*	0.66	1.15	0.96	0.92	0.65	0.75	0.67	0.72	0.55	0.42	0.42
Ti/Ti*	0.77	0.60	0.41	2.19	0.28	1.95	1.86	2.02	0.96	0.93	0.96
δEu	0.96	0.83	0.87	1.04	0.90	1.37	1.31	1.31	1.05	1.09	1.02

Note:

1. Mg# = 100 × Mg/(Mg + Fe^{2+});

2. $(Ce/Ce^*)_{PM} = 2Ce_{PM}/(La_{PM} + Pr_{PM})$; $Nb/Nb^* = 2Nb_{PM}/(Th_{PM} + La_{PM})$; $Ti/Ti^* = 2Ti_{PM}/(Sm_{PM} + Tb_{PM})$; $\delta Eu = Eu/Eu^* = 2Eu_N/(Gd_N + Sm_N)$; PM-primitive mantle normalized; N-chondrite normalized. The normalization values are from Sun and McDonough (1989).

Table 5
Sm–Nd isotopic analyses for metamafic rocks from the Leeuwin Complex.

Sample	Sm (ppm)	Nd (ppm)	$^{147}Sm/^{144}Nd$	$^{143}Nd/^{144}Nd$	±2σ	$f_{Sm/Nd}$	$\varepsilon_{Nd}(0)$	$\varepsilon_{Nd}(t)$	T_{DM} (Ma)
Meta-mafic rocks (t = 670 Ma)									
D09-2	8.3	37.7	0.13309	0.512437	0.000005	-0.32	-3.9	1.5	1347
D13-5	9.21	41.8	0.1332	0.512403	0.000005	-0.32	-4.6	0.8	1412
D31-1	18.3	91.3	0.12117	0.51224	0.000004	-0.38	-7.8	-1.3	1496
D33-1	6.42	29.6	0.13111	0.512329	0.000004	-0.33	-6	-0.4	1513
D34-1	19.3	110	0.10606	0.51221	0.000007	-0.46	-8.3	-0.6	1330
D34-5	4.15	23.5	0.10675	0.512172	0.000004	-0.46	-9.1	-1.4	1392
D34-11	4.48	24.9	0.10876	0.512182	0.000005	-0.45	-8.9	-1.4	1404
D34-12	4.32	25.3	0.10322	0.512192	0.000006	-0.48	-8.7	-0.7	1320
M04-3	10.4	52.3	0.12021	0.512261	0.000006	-0.39	-7.4	-0.8	1447
A06-1	6.01	30.5	0.11912	0.512262	0.000004	-0.39	-7.3	-0.7	1429
A14-4	7.87	40	0.11894	0.512252	0.000006	-0.40	-7.5	-0.9	1442